



HAL
open science

A Data-Driven-based homogenization method to simulate the anisotropic damage of brittle heterogeneous structures

Zakaria Chafia, Julien Yvonnet, Jérémy Bleyer

► To cite this version:

Zakaria Chafia, Julien Yvonnet, Jérémy Bleyer. A Data-Driven-based homogenization method to simulate the anisotropic damage of brittle heterogeneous structures. *Computer Methods in Applied Mechanics and Engineering*, 2025, 437, pp.117747. 10.1016/j.cma.2025.117747 . hal-04908843

HAL Id: hal-04908843

<https://enpc.hal.science/hal-04908843v1>

Submitted on 23 Jan 2025

HAL is a multi-disciplinary open access archive for the deposit and dissemination of scientific research documents, whether they are published or not. The documents may come from teaching and research institutions in France or abroad, or from public or private research centers.

L'archive ouverte pluridisciplinaire **HAL**, est destinée au dépôt et à la diffusion de documents scientifiques de niveau recherche, publiés ou non, émanant des établissements d'enseignement et de recherche français ou étrangers, des laboratoires publics ou privés.

Highlights

A Data-Driven-based homogenization method to simulate the anisotropic damage of brittle heterogeneous structures

Zakaria CHAFIA, Julien YVONNET, Jérémy BLEYER

- A numerical homogenization method for anisotropic damage is proposed using RVE crack simulations as data.
- Operators and internal variables for the macro damage model construction are uniquely defined using Harmonic Analysis of Damage.
- Macro internal variables evolution laws are predicted by a surrogate model using interpolation in the macro strain space.
- A modified strain regularization is proposed at the macro scale to avoid mesh-dependency.
- Anisotropic fracture can be efficiently captured for strongly oriented microstructures at low computational costs in the off-line stage.

A Data-Driven-based homogenization method to simulate the anisotropic damage of brittle heterogeneous structures

Zakaria CHAFIA^{a,b}, Julien YVONNET^a and Jérémy BLEYER^b

^aUniversité Gustave Eiffel, Laboratoire MSME, CNRS, UMR 8208, Marne-la-Vallée, 77454, France

^bEcole des Ponts ParisTech, Laboratoire NAVIER, CNRS, UMR 8205, Champs-sur-Marne, 77420, France

ARTICLE INFO

Keywords:

Multiscale modeling
Computational homogenization
Anisotropic damage
Composite materials
Data-Driven

ABSTRACT


An efficient data-driven multiscale framework for modeling anisotropic damage (M-DDHAD) in heterogeneous structures is proposed, where the anisotropic damage model at the macro scale is constructed purely on the knowledge of Representative Volume Elements (RVE) of the material microstructure. The technique involves three main steps: the construction of a database, obtained by performing off-line calculations of crack propagation on Representative Volume Elements (RVE); the construction of an anisotropic damage model constructed from the database using Harmonic Analysis of Damage and off-line calculations, where damage is computed using the constructed model in tandem with a strain-gradient regularization technique. Using Harmonic Analysis of Damage, an anisotropic damage model defining the evolution of the macroscopic elastic tensor as a function of macro internal variables is provided without specific assumptions about the anisotropy related to the RVE geometry. A surrogate model is constructed to define their evolution. The macroscopic problem uses the constructed anisotropic damage model, and a modified strain-gradient regularization is applied to guarantee mesh-independence. The technique accuracy and robustness has been assessed on several structural problems with different microstructures, involving a strong initial and induced anisotropic fracture behavior, and compared with direct crack numerical simulations (DNS) of heterogeneous structures. Very good accuracy has been obtained both regarding the force-displacement curves as well as crack paths, while keeping the efficiency of classical Finite Element simulations.

1. Introduction

Modelling fracture of heterogeneous materials based on knowledge of their microstructure is a difficult engineering problem, but one that, if mastered, would enable the design of new, more resistant materials, or the optimization of structures to improve their resistance to cracking. The stakes are high for the design of new composites such as 3D woven composites or lightweight materials such as 3D printed architectural materials, among others. Among the difficulties associated with this problem, the strong anisotropy during fracture that can be induced in this type of material makes the simple identification of empirical damage models particularly delicate. In addition, using knowledge of the microstructure as information to build damage models on the scale of the structure involves a homogenization step, which can only be carried out numerically, assuming available a methodology that allows this change of scale, which is still a challenge today. Finally, direct finite element simulations of heterogeneous structures are still limited to small volumes of structures, even using supercomputers, because of the very large scale disparities between the dimensions of the structure and the size of the heterogeneities (fibers, pores, etc.).

Several multiscale methods have been developed in the literature to tackle such problem. In [69, 59, 60, 61, 50, 68], Multiscale Finite Elements Method (MsFEM) [27, 26, 78] was proposed to simulate damage of heterogeneous materials. Within these methods, the computational domain is divided into macroscopic and microscopic regions. Traditional finite element methods are used to solve the equations governing the fracture behavior at the microscopic level using a fine mesh. Then, solutions are mapped to a coarser mesh at the macroscopic level employing multiscale basis functions. Other multiscale approaches are available for simulating heterogeneous structures by integrating different models across various scales. These methods allow to describe the damage in localized regions where the response of the subdomain is coupled with the homogeneous structural model away from the region of interest. For example, the Arlequin method [9, 10] allows incorporating a detailed local model, which captures the fine scale

*Corresponding author

 julien.yvonnet@univ-eiffel.fr (J. YVONNET)

ORCID(s):

phenomena, within a coarser model representing the overall structure. This approach uses weight functions to merge the two scales, ensuring that the fine scale details efficiently influence the coarse scale model, and was applied to damage simulations in [67, 66]. Mesh superposition techniques [58, 11, 48, 65, 19] enable simulating heterogeneous structures by zooming into specific regions of interest. These methods involve conducting an initial coarse scale simulation to obtain a global response of the structure behavior. Then a finer scale model is employed to zoom into these regions for a detailed analysis. The LATIN method [32, 36] and the micro/macro strategy [33, 34, 35] offer an iterative framework to handle nonlinear multiscale problems. This approach addresses interactions across different scales by separating the problem into global and local problems (see [21, 4] for damage simulation applications). In [17], a non-intrusive global/local approach [16] was proposed for simulating damage of heterogeneous structures using the phase field method [6, 46, 53, 45, 44]. This method couples a global model, associated with the overall structure, with a refined local model capturing localized damage phenomena (see also [23, 57, 28]).

Computational homogenization methods constitute an alternative to simulate damage at the structure scale taking into account the microstructure and the evolution of micro cracks. In FE^2 based methods [13, 14, 5, 52], predicting the fracture behavior at the macroscopic scale involves performing simulations on the RVE at the microscopic scale simultaneously. The main drawback of this approach is its computational cost, especially in the case of incremental problems such as damage modelling. Several nonlinear computations are required at each Gauss point of the macroscopic mesh and for all incremental steps, which restrict their use for large scale or industrial applications. To overcome this limitation, various strategies have been developed to accelerate the FE^2 method. In [75, 47, 20, 56], reduced-order models like principal component analysis (PCA) or proper orthogonal decomposition (POD) were used to reduce the RVE computations. More recently, macro clustering, initially [2] and [7] for **inelastic** problems and extended to FE^2 fracture problems in [8], has been introduced by restricting the number of RVE to be computed using k-means clustering on the macro integration points. Another strategy, initiated in [74, 37], involves the use of Data-Driven and machine learning methods for the computational homogenization of nonlinear heterogeneous materials. The key idea of these approaches is the use of surrogate models to substitute RVE computations. A set of offline computations is initially performed at the microscopic scale in a first step. Then, the stored dataset is used to build a surrogate model, which replaces RVE computations for predicting the macroscopic behavior of the structure. These techniques have been applied in numerous studies in the literature. Neural Networks are used in [18, 38, 40, 41, 43]. In [42], a hybrid neural-network-interpolation was used for stochastic multiscale modelling framework. For damage simulation of heterogeneous structure, Data-Driven approaches were used to predict fatigue and fracture in [49]. In [22], a Data-Driven framework for the enhancement of fracture paths in random heterogeneous microstructures was proposed. Predicting delamination of composites using machine learning was suggested in [39, 30]. A multiscale surrogate modelling framework for composite materials considering progressive damage based on artificial neural networks was proposed in [71], as well as damage prediction in fiber-reinforced composites using machine learning in [79, 63]. In [64], machine learning was used to simulate compressive damage in composites laminates. Other approaches have been developed to simulate damage at the structural scale while taking into account the fine scale features, including fracture toughness and characteristic length scale calculations [3], inverse approaches [51] or asymptotic homogenization [12, 72]. See also [54, 55], for homogenization-based multiscale damage modelling of cohesive cracks. **For an in-dept analysis of the behavior of the PC/ABS blends using the computational homogenisation, see [1].**

In this work, a Data-Driven multiscale anisotropic damage modelling method, called M-DDHAD is proposed, to simulate crack nucleation and propagation of **brittle**, heterogeneous, anisotropic structures. The main idea of this approach is to substitute RVE computations by a surrogate model, allowing damage prediction at the structure scale accurately with high efficiency. The proposed M-DDHAD method is carried out in three steps. Initially, a set of offline computations is performed on the RVE using the phase field method [46, 45, 44] to build the database. Next, a harmonic analysis [76, 77] is carried out using the constructed database to compute internal variables and to build their evolution laws and the anisotropic damage model to be used at the macroscopic scale. At the final stage, online computations are performed using the surrogate model to predict the anisotropic damage of heterogeneous structures. Applications to periodic **brittle** composite structures with strongly anisotropic microstructures are presented. The M-DDHAD method is validated using reference computations from damage simulations of full-field periodic heterogeneous structures with a fine description of the microstructure.

2. A Multiscale Data-Driven modeling of anisotropic damage using Harmonic Analysis (M-DDHAD): overview

A data-driven multiscale modelling framework of anisotropic damage (M-DDHAD) method is proposed, where a homogenized anisotropic damage model is constructed purely on the knowledge of Representative Volume Elements (RVE) of the material microstructure. The technique involves three main steps: (i) the construction of a database, obtained by performing off-line calculations of crack propagation in Representative Volume Elements (RVE); (ii) the construction of an anisotropic damage model constructed from the database using Harmonic Analysis of Damage; (iii) On-line calculations, where damage is computed using the constructed model in tandem with a strain-gradient regularization technique. The three main steps of the method are schematically described in Fig. 1 and detailed in the next sections.

3. Off-line calculations

3.1. Micro scale crack modelling

At the microscopic scale, the phase field method is employed to model the damage in the RVE. This approach, initiated in [6], has become a widespread tool to describe crack initiation and propagation in materials. The phase field method, based on minimizing the total energy functional, is able to model arbitrary and complex crack geometries as well as cracks nucleation, coalescence and branching. These advantages provide a highly robust framework to model crack propagation in heterogeneous structures. Let us consider an open domain $\Omega \subset \mathbb{R}^D$ representing a cracked RVE of dimension D and $\partial\Omega$ be the RVE boundary of dimension $D - 1$. Let us consider an open domain $\Omega \subset \mathbb{R}^D$ and its boundary $\partial\Omega$ of dimension $D - 1$. Let $\partial\Omega_u$ and $\partial\Omega_F$ be the parts of the boundary on which Dirichlet and Neumann boundary conditions are prescribed, respectively, such that $\partial\Omega = \partial\Omega_u \cup \partial\Omega_F$ and $\partial\Omega_u \cap \partial\Omega_F = \emptyset$. The total energy functional $\mathcal{E}(\mathbf{u}, d)$, according to [6], is given by:

$$\mathcal{E}(\mathbf{u}, d) = \int_{\Omega} \psi_e(\boldsymbol{\varepsilon}(\mathbf{u}), d) d\Omega + \int_{\Omega} \psi_f(d) d\Omega - \int_{\Omega} \mathbf{f}^* \cdot \mathbf{u} d\Omega - \int_{\partial\Omega_F} \mathbf{F}^* \cdot \mathbf{u} dS, \quad (1)$$

where \mathbf{u} is the displacement field, $\boldsymbol{\varepsilon}(\mathbf{u}) = \frac{1}{2} (\nabla(\mathbf{u}) + \nabla(\mathbf{u})^T)$ is the infinitesimal strain tensor and d is the damage variable; $\psi_e(\mathbf{u}, d)$ denotes the elastic energy density and $\psi_f(d)$ refers to the fracture energy density. \mathbf{f} and \mathbf{F}^* are body forces and prescribed forces on the boundary $\partial\Omega_F$, respectively.

The phase field framework developed in [46, 45, 44] is considered. The elastic energy density, in this model, is split into positive and negative parts using the spectral decomposition of the strain tensor, which is given as:

$$\psi_e(\boldsymbol{\varepsilon}(\mathbf{u}), d) = (g(d)) \psi_e^+(\boldsymbol{\varepsilon}(\mathbf{u})) + \psi_e^-(\boldsymbol{\varepsilon}(\mathbf{u})), \quad (2)$$

in which $g(d) = (1 - d)^2$ is the degradation function applied only on the positive part of the elastic energy density, $\psi_e^+(\boldsymbol{\varepsilon}(\mathbf{u}))$ and $\psi_e^-(\boldsymbol{\varepsilon}(\mathbf{u}))$ refer to the positive and negative parts of the elastic energy density expressed as:

$$\psi_e^{\pm}(\boldsymbol{\varepsilon}(\mathbf{u})) = \frac{\lambda}{2} (\langle \text{Tr}(\boldsymbol{\varepsilon}) \rangle_{\pm})^2 + \mu \text{Tr}((\boldsymbol{\varepsilon}^{\pm})^2), \quad (3)$$

where λ and μ are the Lamé's parameters, $\text{Tr}(\cdot)$ is the trace operator, $\boldsymbol{\varepsilon}^+$ and $\boldsymbol{\varepsilon}^-$ denote the positive and the negative parts of the strain tensors, respectively, which are expressed by:

$$\boldsymbol{\varepsilon}^{\pm} = \sum_{i=1}^k \langle \boldsymbol{\varepsilon}^i \rangle_{\pm} \mathbf{n}^i \otimes \mathbf{n}^i, \quad k = 2, 3, \quad (4)$$

where $\langle x \rangle_{\pm} = \frac{1}{2} (x \pm |x|)$, $\boldsymbol{\varepsilon}^i$ and \mathbf{n}^i are the eigenvalues and eigenvectors of the strain tensor $\boldsymbol{\varepsilon}$.

In this work, the so-called AT2 model [46] is considered for the fracture energy density:

$$\psi_f(d) = \psi_c (d^2 + \ell_0^2 \nabla d \cdot \nabla d), \quad (5)$$

where $\nabla(\cdot)$ is the gradient operator, ℓ_0 is the characteristic length that governs the width of the damage zone, ψ_c is a specific fracture energy density, considered here to be a material property and which can be related to the critical stress

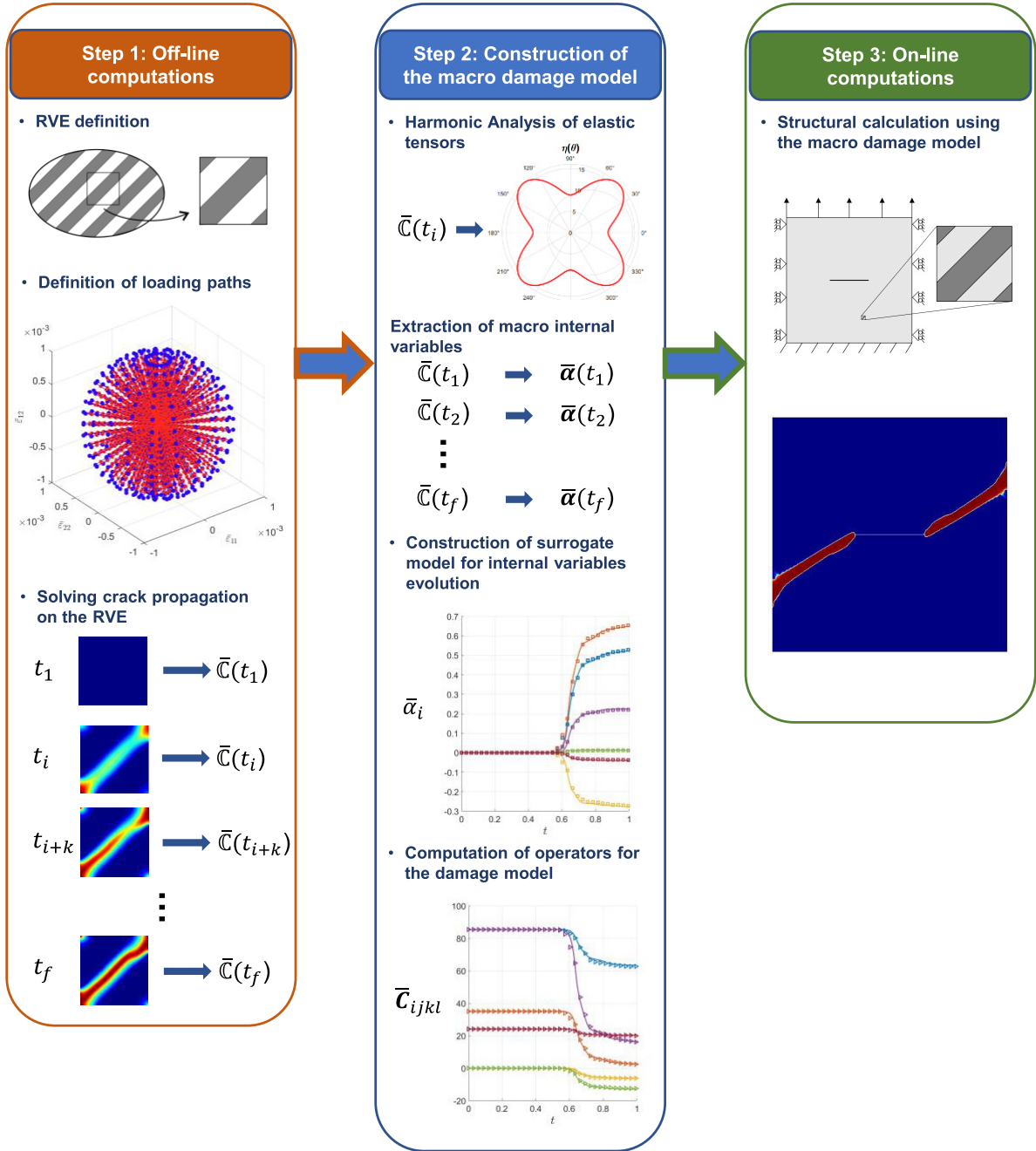


Figure 1: Overview of the M-DDHAD method

σ_c and the fracture toughness G_c by:

$$\psi_c = \frac{\sigma_c^2}{2E} = \frac{G_c}{2\ell_0}, \quad (6)$$

where E is the Young's modulus.

The functional in Eq. (1) is not convex with respect to both unknowns (\mathbf{u} , d), but is convex with respect to each variable separately [70]. To address the minimization of the total energy in Eq. (1), a robust algorithm using a staggered

scheme [46], is considered. Consequently, an incremental problem is obtained, where two coupled sets of equations are solved sequentially. Minimizing (1) with respect to the damage field $d(\mathbf{x})$, the following Euler-Largange equations are obtained:

$$\begin{cases} (1-d)\mathcal{H} - \psi_c \left(d - \ell_0^2 \Delta d \right) = 0 & \text{in } \Omega, \\ d = 1 & \text{on } \Gamma, \\ \nabla d \cdot \mathbf{n} = 0 & \text{on } \partial\Omega, \end{cases}, \quad (7)$$

which are solved by fixing the displacement field \mathbf{u} , and where $\Delta(\cdot)$ is the Laplacian operator, Γ represents the crack surface, \mathbf{n} is the output normal vector on the boundary $\partial\Omega$ and \mathcal{H} refers to the history functional, used to ensure the irreversibility condition [46], defined by:

$$\mathcal{H} = \max_{\tau \in [0, t]} \left[\langle \psi^+(\varepsilon; \tau) - \psi_c \rangle_+ \right]. \quad (8)$$

Minimizing (1) with respect to the displacement field $\mathbf{u}(\mathbf{x})$, the following Euler-Largange equations are obtained:

$$\begin{cases} \nabla \cdot (\boldsymbol{\sigma}) + \mathbf{f} = 0 & \text{in } \Omega, \\ \mathbf{u} = \mathbf{u}^* & \text{on } \partial\Omega_u, \\ \boldsymbol{\sigma} \mathbf{n} = \mathbf{F}^* & \text{on } \partial\Omega_F. \end{cases} \quad (9)$$

which are solved by fixing the damage state $d(\mathbf{x})$. In (9), $\boldsymbol{\sigma} = \frac{\partial W}{\partial \boldsymbol{\varepsilon}}$ is the second-order Cauchy stress tensor, \mathbf{f} are body forces and \mathbf{u}^* and \mathbf{F}^* are prescribed displacements and forces on the corresponding boundaries $\partial\Omega_u$ and $\partial\Omega_F$, respectively. The symbols $\nabla(\cdot)$ and $\nabla \cdot (\cdot)$ denote gradient and divergence operators, respectively. For the strain-density function (3), the constitutive law is expressed (see e.g. [46]) by:

$$\boldsymbol{\sigma} = \left((1-d)^2 + k \right) \left\{ \lambda \langle Tr \boldsymbol{\varepsilon} \rangle_+ \mathbf{1} + 2\mu \boldsymbol{\varepsilon}^+ \right\} + \lambda \langle Tr \boldsymbol{\varepsilon} \rangle_- \mathbf{1} + 2\mu \boldsymbol{\varepsilon}^- \quad (10)$$

where k is a small positive numerical parameter serving to avoid loss of stability in case of fully damaged elements.

In this work, the resolution of Eqs. (7) and (9) is performed employing the classical finite-element method, in quasi-static conditions, using a single iteration at each load increment as in [46]. For a detailed implementation of the phase field method, see e.g. [53]. At each time step, the boundary conditions prescribed on the RVE are given in the form:

$$\mathbf{u}(\mathbf{x}) = \bar{\boldsymbol{\varepsilon}}(t)\mathbf{x} + \tilde{\mathbf{u}}(\mathbf{x}), \quad (11)$$

where $\bar{\boldsymbol{\varepsilon}}(t)$ is defined below, and $\tilde{\mathbf{u}}(\mathbf{x})$ is a periodic function used to ensure boundary conditions on the RVE, and which is enforced through Lagrange multipliers.

3.2. Database construction

In the off-line stage, loading paths are defined, and the equations of the phase field model described in the previous section are solved at each time step and for each loading path, which is proportional from a zero strain and undamaged state until a maximum value of the macro strain tensor $\bar{\boldsymbol{\varepsilon}}(t)$. In the present 2D context, the macro strain space is composed of 3 components, $\bar{\varepsilon}_{11}$, $\bar{\varepsilon}_{22}$ and $\bar{\varepsilon}_{12}$. An ellipsoid is constructed to define the set of macroscopic strains forming the last increment of each proportional load according to:

$$\frac{x^2}{\bar{\varepsilon}_{11}^{max}} + \frac{y^2}{\bar{\varepsilon}_{22}^{max}} + \frac{z^2}{\bar{\varepsilon}_{12}^{max}} = 1 \quad (12)$$

where $\bar{\varepsilon}_{11}^{max}$, $\bar{\varepsilon}_{22}^{max}$ and $\bar{\varepsilon}_{12}^{max}$ denote maximum absolute values of all macroscopic strains components, and:

$$\begin{cases} x = \bar{\varepsilon}_{11}^{max} \cos(\phi) \sin(\varphi) \\ y = \bar{\varepsilon}_{22}^{max} \sin(\phi) \cos(\varphi) \\ z = \bar{\varepsilon}_{12}^{max} \sin(\varphi) \end{cases} \quad \text{with } \phi \in [0, 2\pi] \quad \text{and} \quad \varphi \in \left[-\frac{\pi}{2}, \frac{\pi}{2}\right] \quad (13)$$

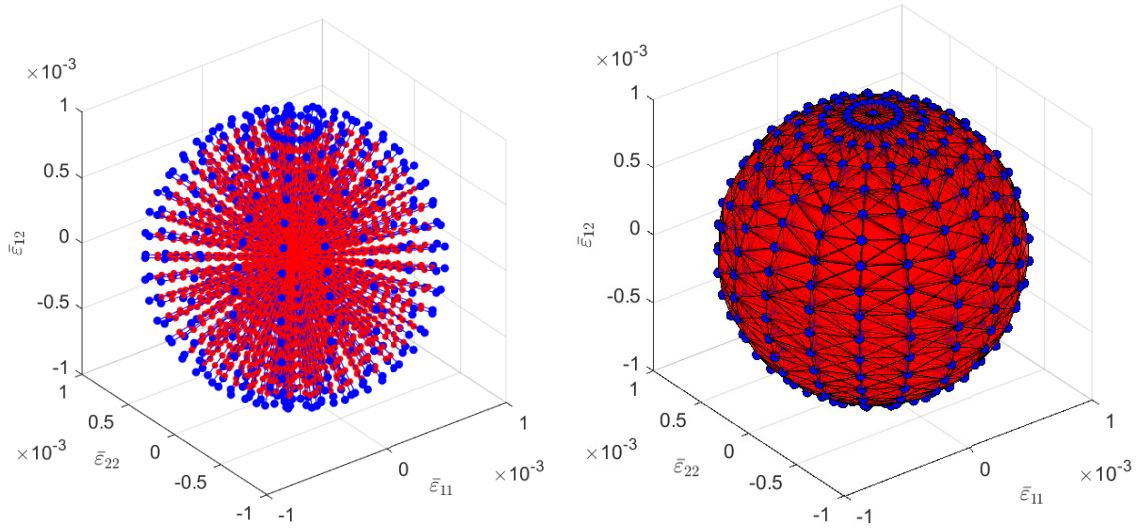


Figure 2: Left: loading paths used during the learning step; right: corresponding tetrahedral mesh for interpolating internal variables.

The number of loading paths n is determined by discretizing the parameter ranges $\phi \in [0, 2\pi]$ and $\varphi \in [-\frac{\pi}{2}, \frac{\pi}{2}]$. Each loading path initiates from the ellipsoid center which has the coordinates $\bar{\epsilon}_n = (0, 0, 0)$ towards the final macroscopic strain associated with $\bar{\epsilon}_n^{max}$ (see Fig. 2): each blue point depicts the final macroscopic strain of each loading path and the red points refer to intermediate strain states. Note that the above loading paths induce both traction and compression states, to take into account both situations during the on-line simulations.

For each strain state, Eqs. (7)-(9) are solved. Then, given the damage state $d(\mathbf{x}, t)$ in the RVE, the effective elastic tensor is computed through elastic homogenization according to:

$$\bar{\mathbb{C}}(t) = \frac{1}{|\Omega|} \int_{\Omega} \mathbb{C}(\mathbf{x}, d(t)) : \mathbb{A}(\mathbf{x}, t) d\Omega, \quad (14)$$

where $|\Omega|$ is the volume of Ω , $\mathbb{A}(\mathbf{x}, t)$ is the localization tensor at time t and for a "frozen" $d(\mathbf{x}, t)$ distribution, defined by:

$$A_{ijkl}(\mathbf{x}, t) = \epsilon_{ij}^{(kl)}(\mathbf{x}, t), \quad (15)$$

where $\epsilon_{ij}^{(kl)}(\mathbf{x})$ is the strain solution of the problem (9) for $\bar{\epsilon} = \frac{1}{2} (\mathbf{e}_k \otimes \mathbf{e}_l + \mathbf{e}_l \otimes \mathbf{e}_k)$ and for the fixed $\mathbb{C}(\mathbf{x}, d(t))$.

Next, each elastic tensor $\bar{\mathbb{C}}(t)$ is stored for each macro-strain state $\bar{\epsilon}(t)$, forming the database. Note that each loading path being independent, these off-line calculations can be efficiently performed in parallel.

4. Construction of the macro model

4.1. Damage model based on harmonic analysis of elasticity tensors

To construct the macroscopic anisotropic damage model, the Data-Driven Harmonic Analysis Damage framework as proposed in [76, 77] is adopted here. In this context, the elastic tensor at time t can be defined according to:

$$\bar{\mathbb{C}}(t) = \bar{\mathbb{C}}_0 - \sum_{k=1}^L \bar{\alpha}_k(t) \tilde{\mathbb{C}}_k \quad (16)$$

where $\bar{\mathbb{C}}_0$ is the undamaged homogenized tensor of the RVE, and L is the number of independent elastic constants in $\bar{\mathbb{C}}(t)$, i.e. $L = 6$ in 2D and $L = 21$ in 3D. Above, $\tilde{\mathbb{C}}_k$ are fourth-order elastic tensors (see [77]) and $\bar{\alpha}_k$ denote the macro damage variables, which are defined as follows. An expression of the matrix form for $\tilde{\mathbb{C}}_k$ is provided in 2D in Appendix B.

It was shown in [31, 24, 25] that any elastic tensor can be characterized by two orientation distribution functions (ODFs):

$$\eta(\mathbf{n}, t) = n_i n_j n_k n_l \bar{C}_{ijkl}(t), \quad \kappa(\mathbf{n}, t) = \delta_{ij} n_k n_l \bar{C}_{ijkl}(t), \quad (17)$$

where \mathbf{n} is a unitary orientation vector normal to the unit sphere. In the case of isotropic materials, the functions $\eta(\mathbf{n})$ and $\kappa(\mathbf{n})$ are constant.

Anisotropic damage can then be defined in the same way using two ODFs [31, 24, 25] as:

$$d(\mathbf{n}, t) = 1 - \frac{\eta(\mathbf{n}, t)}{\eta_0(\mathbf{n})}, \quad h(\mathbf{n}, t) = 1 - \frac{\kappa(\mathbf{n}, t)}{\kappa_0(\mathbf{n})} \quad (18)$$

where $\eta_0(\mathbf{n})$ and $\kappa_0(\mathbf{n})$ are given by:

$$\eta_0(\mathbf{n}) = n_i n_j n_k n_l \bar{C}_{0ijkl}, \quad \kappa_0(\mathbf{n}) = \delta_{ij} n_k n_l \bar{C}_{0ijkl}. \quad (19)$$

In the context of harmonic analysis of damage, the ODFs are expanded into Fournier series as:

$$d(\mathbf{n}, t) = d_0(t) + \mathbf{D}(t) : \mathbf{F}(\mathbf{n}) + \mathbb{D}(t) :: \mathbb{F}(\mathbf{n}), \quad (20a)$$

$$h(\mathbf{n}, t) = h_0(t) + \mathbf{D}(t) : \mathbf{F}(\mathbf{n}), \quad (20b)$$

where $d_0(t)$ and $h_0(t)$ denote scalar coefficients, $\mathbf{D}(t)$ and $\mathbb{D}(t)$ denote second- and fourth-order coefficients, and $\{1, \mathbf{F}(\mathbf{n}), \mathbb{F}(\mathbf{n})\}$ are generalized spherical harmonics that form a complete orthonormal basis [29]. Above, $\mathbf{A} : \mathbf{B} = A_{ij} B_{ij}$ and $\mathbb{D} :: \mathbb{F} = D_{ijkl} F_{ijkl}$. The expression of these operators can be found in Appendix A in 2D and in 3D in [77]. In (20a)-(20b), there are only L independent coefficients α_k in $d_0(t)$, $h_0(t)$, \mathbf{D} and \mathbb{D} [24], which are chosen here as the macro internal variables. A more compact form for these spherical harmonic expansions can be written as [77]:

$$d(\mathbf{n}, t) = \sum_{k=1}^L V_k^d(\mathbf{n}) \bar{\alpha}_k(t), \quad h(\mathbf{n}, t) = \sum_{k=1}^L V_k^h(\mathbf{n}) \bar{\alpha}_k(t), \quad (21)$$

where the expressions of \mathbf{V}^d and \mathbf{V}^h are provided in 2D in Appendix B and in 3D in [77].

In 2D, the set of macro internal variables is defined by:

$$\bar{\alpha}(t) = \{\bar{\alpha}_1(t), \bar{\alpha}_2(t), \bar{\alpha}_3(t), \bar{\alpha}_4(t), \bar{\alpha}_5(t), \bar{\alpha}_6(t)\}, \quad (22)$$

with [77]:

$$\bar{\alpha}_1 = d_0, \quad \bar{\alpha}_2 = h_0, \quad \bar{\alpha}_3 = D_{11}, \quad \bar{\alpha}_4 = D_{12}, \quad \bar{\alpha}_5 = D_{1111}, \quad \bar{\alpha}_6 = D_{1112}. \quad (23)$$

where the expressions of $d(t)$, $h(t)$, $\mathbf{D}(t)$ and $\mathbb{D}(t)$ are provided in Appendix A.

4.2. Construction of macro internal variables evolution laws

In this work, a surrogate model is constructed to define the evolution of the macroscopic internal variables. For each time step t , a set of macro internal variables $\bar{\alpha}(t)$ is computed from the corresponding homogenized elastic tensors $\bar{\mathbb{C}}(t)$ obtained from (14), associated with a macroscopic strain $\bar{\epsilon}(t)$. Then, the surrogate model relates the macro strains $\bar{\epsilon}(t)$ and the set of internal variables $\bar{\alpha}(t)$ during the proportional loads:

$$\bar{\alpha}(t) = \mathcal{F}(\bar{\epsilon}(t)). \quad (24)$$

For this purpose, the set of points constructed during the definition of loading paths (see Fig. 2) is used to construct a tetrahedral mesh in the macro strain space $\{\bar{\epsilon}_{11}, \bar{\epsilon}_{22}, \bar{\epsilon}_{12}\}$ using a Delaunay tessellation. To evaluate the internal variables for a given macro strain, the values of internal variables are interpolated from the data $\bar{\alpha}_i$ points which form the nodes of the tetrahedral mesh according to:

$$\bar{\alpha}(\bar{\epsilon}_{11}, \bar{\epsilon}_{22}, \bar{\epsilon}_{12}) = \sum_i N_i(\bar{\epsilon}_{11}, \bar{\epsilon}_{22}, \bar{\epsilon}_{12}) \bar{\alpha}_i, \quad (25)$$

where N_i are the finite element shape functions of the tetrahedral mesh. Note that for a 3D problem, the strain space would be 6-dimensional, and would require another approximation construction, such as radial basis or neural networks. As an important assumption, the above surrogate model only holds here for monotonous loadings. The treatment of loading/unloading cases is out of the scope of the present work and will deserve further developments.

5. On-line calculations

Given the macro anisotropic damage model and the internal variables evolution laws, a solving procedure for the macro scale problem is proposed.

Let us consider an open domain $\bar{\Omega} \subset \mathbb{R}^D$ and its boundary $\partial\bar{\Omega}$ of dimension $D - 1$. Let $\partial\bar{\Omega}_{\bar{u}}$ and $\partial\bar{\Omega}_{\bar{F}}$ be the parts of the boundary on which Dirichlet and Neumann boundary conditions are prescribed, respectively, such that $\partial\bar{\Omega} = \partial\bar{\Omega}_{\bar{u}} \cup \partial\bar{\Omega}_{\bar{F}}$ and $\partial\bar{\Omega}_{\bar{u}} \cap \partial\bar{\Omega}_{\bar{F}} = \emptyset$. The macroscopic elastic energy is defined by:

$$\bar{\mathcal{E}}(\bar{\mathbf{u}}, \bar{\boldsymbol{\alpha}}) = \int_{\bar{\Omega}} \bar{\psi}_e(\bar{\boldsymbol{\varepsilon}}(\bar{\mathbf{u}}), \bar{\boldsymbol{\alpha}}) d\bar{\Omega} - \int_{\bar{\Omega}} \bar{\mathbf{f}} \cdot \delta\bar{\mathbf{u}} d\bar{\Omega} - \int_{\partial\bar{\Omega}_{\bar{F}}} \bar{\mathbf{F}}^* \cdot \delta\bar{\mathbf{u}} d\bar{\Omega} \quad (26)$$

where $\bar{\mathbf{u}}$ is the macroscopic displacement field, $\bar{\boldsymbol{\varepsilon}}(\bar{\mathbf{u}}) = \frac{1}{2} (\nabla(\bar{\mathbf{u}}) + \nabla(\bar{\mathbf{u}})^T)$ is the macroscopic infinitesimal strain tensor, $\bar{\mathbf{f}}$ and $\bar{\mathbf{F}}^*$ are body forces and prescribed surface forces on the boundary $\partial\bar{\Omega}_{\bar{F}}$, respectively. $\bar{\psi}_e(\bar{\mathbf{u}}, \bar{\boldsymbol{\alpha}})$ denotes the macroscopic elastic energy density defined by:

$$\bar{\psi}_e(\bar{\boldsymbol{\varepsilon}}(\bar{\mathbf{u}}), \bar{\boldsymbol{\alpha}}) = \frac{1}{2} \bar{\boldsymbol{\varepsilon}}(\bar{\mathbf{u}}) : \bar{\mathbb{C}}(\bar{\boldsymbol{\alpha}}) : \bar{\boldsymbol{\varepsilon}}(\bar{\mathbf{u}}) \quad (27)$$

where $\bar{\mathbb{C}}(\bar{\boldsymbol{\alpha}})$ is given by (16).

Minimizing (26) with respect to the macro displacements $\bar{\mathbf{u}}$ with evolution laws for the macro internal variables (25) results into a local damage model. To avoid well-known mesh dependency related to such models, a revisited strain regularization with a damage-dependent transient length scale, adapted to the framework of this work, is introduced and described in the following. At each macro time t (quasi-static loading evolution), an alternate solving procedure is developed, where the macro displacement problem is first solved, given the macro internal damage variables $\bar{\boldsymbol{\alpha}}$, and then a regularization problem is solved, where given the macro displacements $\bar{\mathbf{u}}$, the internal variables $\bar{\boldsymbol{\alpha}}$ are solved. Each problem is described in the next sections.

5.1. Mechanical problem

5.1.1. Governing equations

Given the macro damage internal variables $\bar{\boldsymbol{\alpha}}$, minimizing the energy functional (26) with respect to the macroscopic displacement field gives: find $\bar{\mathbf{u}} \in \bar{\mathcal{U}} = \left\{ \bar{\mathbf{u}} \in H^1(\bar{\Omega}) \mid \bar{\mathbf{u}} = \bar{\mathbf{u}}^* \text{ on } \partial\bar{\Omega}_{\bar{u}} \right\}$ such that

$$\forall \delta\bar{\mathbf{u}} \in \bar{\mathcal{U}}^0 = \left\{ \delta\bar{\mathbf{u}} \in H^1(\bar{\Omega}) \mid \delta\bar{\mathbf{u}} = 0 \text{ on } \partial\bar{\Omega}_{\bar{u}} \right\}, \quad D_{\delta\bar{\mathbf{u}}} \bar{\mathcal{E}}(\bar{\mathbf{u}}, \bar{\boldsymbol{\alpha}}) = 0, \quad (28)$$

where

$$D_{\delta\bar{\mathbf{u}}} \bar{\mathcal{E}}(\bar{\mathbf{u}}, \bar{\boldsymbol{\alpha}}) = \int_{\bar{\Omega}} \bar{\boldsymbol{\sigma}}(\bar{\boldsymbol{\varepsilon}}(\bar{\mathbf{u}}), \bar{\boldsymbol{\alpha}}) : \bar{\boldsymbol{\varepsilon}}(\delta\bar{\mathbf{u}}) d\bar{\Omega} - \int_{\bar{\Omega}} \bar{\mathbf{f}} \cdot \delta\bar{\mathbf{u}} d\bar{\Omega} - \int_{\partial\bar{\Omega}_{\bar{F}}} \bar{\mathbf{F}}^* \cdot \delta\bar{\mathbf{u}} d\bar{\Omega}, \quad (29)$$

where $\bar{\boldsymbol{\sigma}}(\bar{\boldsymbol{\varepsilon}}(\bar{\mathbf{u}}), \bar{\boldsymbol{\alpha}})$ denotes the macroscopic stress tensor, defined by:

$$\bar{\boldsymbol{\sigma}}(\bar{\boldsymbol{\varepsilon}}(\bar{\mathbf{u}}), \bar{\boldsymbol{\alpha}}) = \frac{\partial \bar{\psi}_e}{\partial \bar{\boldsymbol{\varepsilon}}}(\bar{\boldsymbol{\varepsilon}}(\bar{\mathbf{u}}), \bar{\boldsymbol{\alpha}}). \quad (30)$$

The Euler-Lagrange equations associated with Eq. (28) are given by:

$$\begin{cases} \nabla \cdot (\bar{\boldsymbol{\sigma}}) + \bar{\mathbf{f}} = 0 & \text{in } \bar{\Omega}, \\ \bar{\mathbf{u}} = \bar{\mathbf{u}}^* & \text{on } \partial\bar{\Omega}_{\bar{u}}, \\ \bar{\boldsymbol{\sigma}} \bar{\mathbf{n}} = \bar{\mathbf{F}}^* & \text{on } \partial\bar{\Omega}_{\bar{F}}, \end{cases} \quad (31)$$

in which $\bar{\mathbf{n}}$ is the unitary normal vector to the boundary $\partial\bar{\Omega}$.

Using Eqs. (27) and (30), it yields:

$$\bar{\boldsymbol{\sigma}}(\bar{\boldsymbol{\varepsilon}}(\bar{\mathbf{u}}), \bar{\boldsymbol{\alpha}}) = \bar{\mathbb{C}}(\bar{\boldsymbol{\alpha}}) : \bar{\boldsymbol{\varepsilon}}(\bar{\mathbf{u}}). \quad (32)$$

The weak form of the displacement problem (31) can be thus expressed as:

$$\forall \delta\bar{\mathbf{u}} \in \bar{\mathcal{U}}^0, \quad \int_{\bar{\Omega}} \bar{\boldsymbol{\varepsilon}}(\bar{\mathbf{u}}) : \bar{\mathbb{C}}(\bar{\boldsymbol{\alpha}}) : \bar{\boldsymbol{\varepsilon}}(\delta\bar{\mathbf{u}}) d\bar{\Omega} = \int_{\bar{\Omega}} \bar{\mathbf{f}} \cdot \delta\bar{\mathbf{u}} d\bar{\Omega} + \int_{\partial\bar{\Omega}_{\bar{F}}} \bar{\mathbf{F}}^* \cdot \delta\bar{\mathbf{u}} d\bar{\Omega}. \quad (33)$$

5.1.2. Finite-element discretization

The macroscopic displacement field, the macroscopic strain tensor and their variations can be approximated in one element by:

$$\bar{\mathbf{u}} = \bar{\mathbf{N}}_u \bar{\mathbf{u}}_i \quad ; \quad \delta \bar{\mathbf{u}} = \bar{\mathbf{N}}_u \delta \bar{\mathbf{u}}_i \quad ; \quad \bar{\boldsymbol{\varepsilon}}(\bar{\mathbf{u}}) = \bar{\mathbf{B}}_u \bar{\mathbf{u}}_i \quad ; \quad \bar{\boldsymbol{\varepsilon}}(\delta \bar{\mathbf{u}}) = \bar{\mathbf{B}}_u \delta \bar{\mathbf{u}}_i, \quad (34)$$

where $\bar{\mathbf{u}}_i$ are the nodal values of the macroscopic displacement field $\bar{\mathbf{u}}$, $\bar{\mathbf{N}}_u$ and $\bar{\mathbf{B}}_u$ are matrices of displacement shape functions and of displacement shape functions derivatives associated to the macro-mesh, respectively.

The discretization of the mechanical problem (33) leads to the following discrete system of equations:

$$\bar{\mathbf{K}}_u \bar{\mathbf{u}} = \bar{\mathbf{F}}_u, \quad (35)$$

in which

$$\bar{\mathbf{K}}_u = \int_{\bar{\Omega}} \bar{\mathbf{B}}_u^T \bar{\mathbf{C}}(\bar{\boldsymbol{\alpha}}) \bar{\mathbf{B}}_u d\bar{\Omega}, \quad (36)$$

and

$$\bar{\mathbf{F}}_u = \int_{\bar{\Omega}} \bar{\mathbf{N}}_u^T \bar{\mathbf{f}} d\bar{\Omega} + \int_{\partial \bar{\Omega}_F} \bar{\mathbf{N}}_u^T \bar{\mathbf{F}}^* d\bar{S}. \quad (37)$$

5.2. Damage problem

5.2.1. Governing equations

Following [62, 15], a revisited strain regularization with a damage-dependent transient length scale, adapted to the framework of this work, is introduced. The approach involves solving differential equations including higher-order derivatives of the strain tensor, which are expressed as follow:

$$\bar{\boldsymbol{\varepsilon}} = \tilde{\boldsymbol{\varepsilon}} - \frac{1}{2} (1 - d_{\theta}^{max}) \bar{\ell}_0^2 \Delta \tilde{\boldsymbol{\varepsilon}} \quad (38)$$

where, $\bar{\boldsymbol{\varepsilon}}$ is the macroscopic strain computed using the displacement field $\bar{\mathbf{u}}$, $\tilde{\boldsymbol{\varepsilon}}$ is the macroscopic regularized strain and $\bar{\ell}_0$ denotes the characteristic length at the macroscopic scale. In Eq. (38), d_{θ}^{max} is the maximum of the damage orientation function $d(\theta)$ given by (21)-(66) with respect to the orientation θ , given as:

$$d_{\theta}^{max} = \max_{\theta \in [-\pi, \pi]} d(\theta). \quad (39)$$

Multiplying (38) by an arbitrary function $\delta \bar{\boldsymbol{\varepsilon}}_{ij}$ for each component $\bar{\boldsymbol{\varepsilon}}_{ij}$ and integrating over $\bar{\Omega}$ we obtain:

$$\int_{\bar{\Omega}} \bar{\boldsymbol{\varepsilon}}_{ij} \delta \tilde{\boldsymbol{\varepsilon}}_{ij} d\bar{\Omega} = \int_{\bar{\Omega}} \tilde{\boldsymbol{\varepsilon}}_{ij} \delta \tilde{\boldsymbol{\varepsilon}}_{ij} d\bar{\Omega} - \int_{\bar{\Omega}} \frac{1}{2} (1 - d_{\theta}^{max}) \bar{\ell}_0^2 \Delta \tilde{\boldsymbol{\varepsilon}}_{ij} \delta \tilde{\boldsymbol{\varepsilon}}_{ij} d\bar{\Omega}. \quad (40)$$

Using the property:

$$\Delta \tilde{\boldsymbol{\varepsilon}}_{ij} \delta \tilde{\boldsymbol{\varepsilon}}_{ij} = \nabla \cdot (\nabla \tilde{\boldsymbol{\varepsilon}}_{ij} \delta \tilde{\boldsymbol{\varepsilon}}_{ij}) - \nabla \tilde{\boldsymbol{\varepsilon}}_{ij} \cdot \nabla \delta \tilde{\boldsymbol{\varepsilon}}_{ij}, \quad (41)$$

and the divergence theorem, as well as assuming the natural boundary condition $\nabla \tilde{\boldsymbol{\varepsilon}}_{ij} \cdot \mathbf{n} = 0$ on $\delta \bar{\Omega}$. the weak form corresponding to Eq. (38) can be rewritten as:

$$\forall \delta \tilde{\boldsymbol{\varepsilon}}_{ij} \in H^1(\bar{\Omega}), \quad \int_{\bar{\Omega}} \bar{\boldsymbol{\varepsilon}}_{ij} \delta \tilde{\boldsymbol{\varepsilon}}_{ij} d\bar{\Omega} = \int_{\bar{\Omega}} \tilde{\boldsymbol{\varepsilon}}_{ij} \delta \tilde{\boldsymbol{\varepsilon}}_{ij} d\bar{\Omega} + \int_{\bar{\Omega}} \frac{1}{2} (1 - d_{\theta}^{max}) \bar{\ell}_0^2 \nabla \tilde{\boldsymbol{\varepsilon}}_{ij} \cdot \nabla (\delta \tilde{\boldsymbol{\varepsilon}}_{ij}) d\bar{\Omega}. \quad (42)$$

The internal variables $\bar{\boldsymbol{\alpha}}_i$ are then computed from Eq. (25) taking as input the regularized macroscopic strain $\tilde{\boldsymbol{\varepsilon}}$.

5.2.2. Finite-element discretization

The macroscopic strain tensor components, the macroscopic strain tensor gradient components and their variations can be approximated in one element by:

$$\tilde{\epsilon}_{ij} = \overline{\mathbf{N}}_{\epsilon} \tilde{\epsilon}_{ij}^k ; \quad \delta \tilde{\epsilon}_{ij} = \overline{\mathbf{N}}_{\epsilon} \delta \tilde{\epsilon}_{ij}^k ; \quad \nabla \tilde{\epsilon}_{ij} = \overline{\mathbf{B}}_{\epsilon} \tilde{\epsilon}_{ij}^k ; \quad \nabla (\delta \tilde{\epsilon}_{ij}) = \overline{\mathbf{B}}_{\epsilon} \delta \tilde{\epsilon}_{ij}^k, \quad (43)$$

where $\tilde{\epsilon}_{ij}^k$ are the nodal values of the macroscopic strain tensor components $\tilde{\epsilon}_{ij}$, $\overline{\mathbf{N}}_{\epsilon}$ and $\overline{\mathbf{B}}_{\epsilon}$ are vectors and matrices of shape functions and of shape functions derivatives for scalar fields, associated to the macro-mesh, respectively.

The discretization of the regularization problem (42) leads to the following discrete systems of equations:

$$\overline{\mathbf{K}}_{\epsilon} \tilde{\epsilon}_{ij} = \overline{\mathbf{F}}_{\epsilon}^{ij}, \quad ij = 11, 22, 12, \quad (44)$$

in which

$$\overline{\mathbf{K}}_{\epsilon} = \int_{\Omega} \overline{\mathbf{N}}_{\epsilon}^T \overline{\mathbf{N}}_{\epsilon} + \frac{1}{2} (1 - d_{\theta}^{max}) \overline{\mathcal{L}}_0^2 \overline{\mathbf{B}}_{\epsilon}^T \overline{\mathbf{B}}_{\epsilon} d\Omega, \quad (45)$$

and

$$\overline{\mathbf{F}}_{\epsilon}^{ij} = \int_{\Omega} \overline{\mathbf{N}}_{\epsilon}^T \tilde{\epsilon}_{ij} d\Omega \quad (46)$$

5.3. M-DDHAD algorithm: summary

The M-DDHAD method algorithm is summarized in Algorithm 1.

6. Numerical applications and method validation

In this section, numerical applications of crack nucleation and propagation, using the proposed M-DDHAD method, are presented. First, two applications of the stiffness tensor reconstruction of a damaged RVE are provided. Then, examples of damage modeling of heterogeneous structures with periodic microstructure are presented. Homogenized model results are validated through comparison with reference computations from damage simulations using full-field periodic heterogeneous structures with a fine description of the microstructure.

6.1. Reconstruction of the stiffness matrix $\overline{\mathbf{C}}(t)$

This section presents two applications of the stiffness matrix reconstruction. For both applications, the RVE is a square with inclusion of dimensions $L \times L = 1 \times 1$ mm² for the plate, and the inclusion radius is $r = 0.2$ mm (see Fig. 17b). The mechanical properties of the microstructure are as follows: $E_m = 52$ GPa, $\nu_m = 0.3$ et $\sigma_c^m = 30$ MPa for the matrix, and $E_i = 10000$ GPa, $\nu_i = 0.3$ et $\sigma_c^i = 10000$ GPa for the inclusion. For all examples in this work, the microscopic mesh is composed of structured quadrilateral elements of size $h = 0.01$ mm. The stiffness matrix $\overline{\mathbf{C}}_0$ associated with the tensor $\overline{\mathbf{C}}_0$ and the matrix $\tilde{\mathbf{C}}$ (see Eq. (61)) are given as:

$$\overline{\mathbf{C}}_0 = \begin{bmatrix} 85.38 & 35.00 & 0 \\ 35.00 & 85.38 & 0 \\ 0 & 0 & 24.10 \end{bmatrix}, \quad (47)$$

and

$$\tilde{\mathbf{C}} = \begin{bmatrix} 85.38 & 0 & 85.11 & 0 & 85.11 & 0 \\ -85.38 & 120.38 & 0 & 0 & -85.11 & 0 \\ 0 & 0 & 0 & 42.28 & 0 & 84.83 \\ 85.38 & 0 & -85.11 & 0 & 85.11 & 0 \\ 0 & 0 & 0 & 42.28 & 85.11 & -84.83 \\ 84.29 & -60.19 & 0 & 0 & -84.56 & 0 \end{bmatrix}. \quad (48)$$

Algorithm 1 The M-DDHAD method

-
- 1: **Offline Computations**
 - 2: Define the RVE geometry and construct its mesh.
 - 3: Construct the ellipsoid of loading paths by (12), (13).
 - 4: **for** each loading path k **do**
 - 5: **for** $t_n \leq T$ **do**
 - 6: Solve the microscopic problem (section 3.1).
 - 7: Compute and store $\bar{\mathbf{C}}^k(t_n)$.
 - 8: **end for**
 - 9: **end for**
 - 10:
 - 11: **Scale transition: Micro to Macro scale**
 - 12: Harmonic analysis of damage, compute $\bar{\alpha}$ by (23).
 - 13: Construct the evolution laws $\bar{\alpha} = f_i(\bar{\epsilon})$.
 - 14: Construct the operators of the anisotropic damage model: $\bar{\mathbf{C}}^0$, $\tilde{\mathbf{C}}$ from (14) and (60).
 - 15:
 - 16: **Online Computations**
 - 17: Define the structure geometry and construct its mesh.
 - 18: **for** $\bar{t}_{m+1} \leq \bar{T}$ **do**
 - 19: Given $\bar{\alpha}^m$ at load increment \bar{t}_m .
 - 20: **Compute displacement:**
 - 21: Compute $\bar{\mathbf{C}}(\bar{\alpha}^m)$ by (16).
 - 22: Compute and assemble $\bar{\mathbf{K}}_{\bar{u}}$ and $\bar{\mathbf{F}}_{\bar{u}}$ by (36), (37).
 - 23: Compute macroscopic displacement $\bar{\mathbf{u}}_{m+1}$ by solving (35).
 - 24: Compute macroscopic strain $\bar{\epsilon}_{m+1}$.
 - 25: **Compute damage:**
 - 26: Compute $\bar{d}(\theta, \bar{t}_m)$ and $\bar{d}_{\theta}^{max}(\bar{t}_m)$ by (21), (39).
 - 27: Compute and assemble $\bar{\mathbf{K}}_{\bar{\epsilon}}$ and $\bar{\mathbf{F}}_{\bar{\epsilon}}$ by (45), (46).
 - 28: Compute the regularized macroscopic strain $\tilde{\epsilon}_{m+1}$ by solving (44).
 - 29: Compute macroscopic damage variables $\bar{\alpha}^{m+1}$ by Eq. (25).
 - 30: **end for**
-

The first application focuses on the DDHAD method (Data-Driven Harmonic Analysis of Damage) and its improved version [76, 77]. The aim is to illustrate, through damage modeling of the RVE, the reconstruction of the stiffness tensor evolution $\bar{\mathbf{C}}(t)$ as a function of internal variables $\bar{\alpha}_i(t)$, where t is a pseudo time parameter describing the load evolution. The damage simulation is carried out, subjecting the RVE to periodic boundary conditions, using the macroscopic strain given by:

$$\bar{\epsilon}(t) = 10^{-4} \times \begin{bmatrix} 2.56 & -2.84 \\ -2.84 & 0.69 \end{bmatrix} t, \quad (49)$$

where the pseudo time $t \in [0, 1]$. The loading step used in this simulation is $\Delta t = 5.10^{-3}$ (200 loading increments). The regularization length, in this case, is chosen as $\ell_0 = 0.02$ mm.

Fig. 3 illustrates the final damage state of the RVE ($t = 1$) associated with the macroscopic strain in Eq. (49). Fig. 4a shows the evolution of the extracted internal variables $\bar{\alpha}_i(t)$ using the procedure described in Eq. (23) and Appendix A. Unlike classical damage variable ranging between 0 and 1, internal variables $\bar{\alpha}_i(t)$ do not necessarily vary between 0 and 1, and can take negative values. Notably, in this case, the first three internal variables $\bar{\alpha}_1(t)$, $\bar{\alpha}_2(t)$ and $\bar{\alpha}_3(t)$ are positive and increasing, while the others ($\bar{\alpha}_4(t)$, $\bar{\alpha}_5(t)$ and $\bar{\alpha}_6(t)$) are negative and decreasing. It can also be noted that the internal variables $\bar{\alpha}_5(t)$ and $\bar{\alpha}_6(t)$ have very small values. Fig. 4b shows the evolution of the components of the stiffness matrix associated with the damaged RVE. On the one hand, the components are directly computed by numerical simulation using the phase field method [46, 45, 44] combined with the numerical homogenization technique in [73]. On the

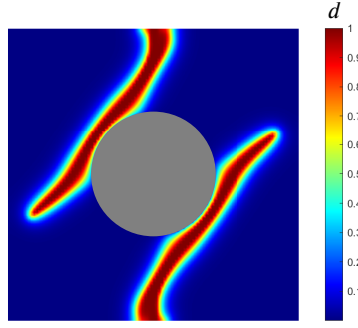


Figure 3: Final damage state of the RVE ($t = 1$) associated to the macroscopic strain in the Eq. (49).

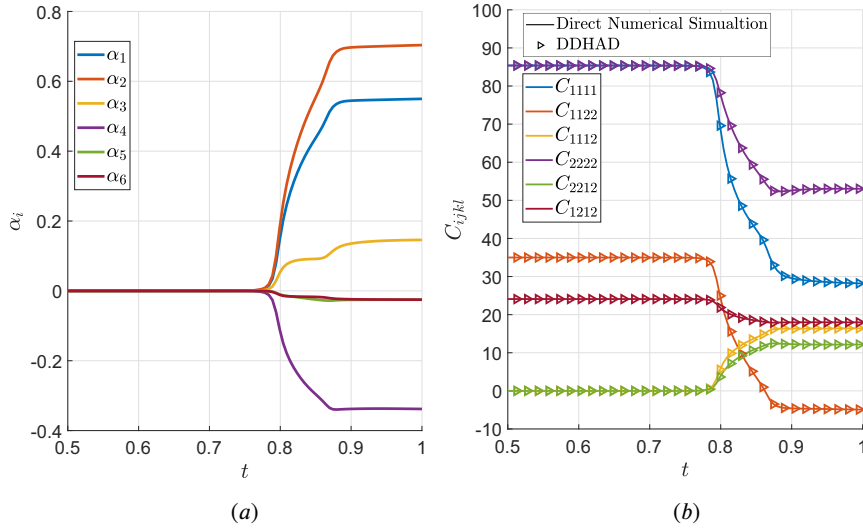


Figure 4: RVE damage evolution ($t \in [0.5, 1]$): (a) Internal variables evolution; (b) Stiffness matrix components evolution: DDHAD vs Direct Numerical Simulation.

other hand, the stiffness matrix is reconstructed based on the extracted internal variables evolution according to the anisotropic damage model in Eq. (16). It is quite remarkable that the reconstructed stiffness tensor evolution shows an excellent alignment with that of the directly computed stiffness tensor. This result demonstrates that the anisotropic damage model in Eq. (16), with six internal variables $\bar{\alpha}_i(t)$, is very accurate to describe the induced anisotropic damage in this example.

The second application demonstrates the ability of the proposed M-DDHAD method to accurately predict the evolution of internal variables, as well as the evolution of the stiffness matrix components. The surrogate model is built using offline damage simulations on the RVE using the loading step $\Delta t = 5 \cdot 10^{-3}$ (200 loading increments) with 500 loading paths. The regularization length is $\ell_0 = 0.06$ mm. The database is constructed from the maximum macroscopic strain:

$$\bar{\epsilon}_{max} = 10^{-4} \times \begin{bmatrix} 6 & 7 \\ 7 & 6 \end{bmatrix}. \quad (50)$$

The validation is performed by subjecting the RVE to periodic boundary conditions (11), using a macroscopic strain path that is not part of offline computations loading paths as:

$$\bar{\epsilon}(t) = 10^{-4} \times \begin{bmatrix} -1.12 & 2.13 \\ 2.13 & 5.47 \end{bmatrix} t, \quad (51)$$

where the pseudo time $t \in [0, 1]$. The loading step used in this validation simulation is $\Delta t = 5 \cdot 10^{-3}$ (200 loading increments).

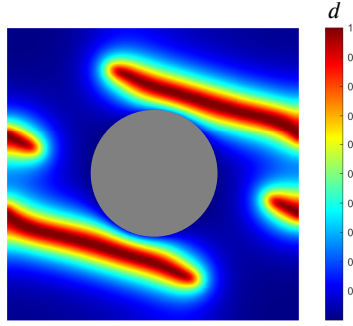


Figure 5: Final damage state of the RVE ($t = 1$) associated to the macroscopic strain in the Eq. (51).

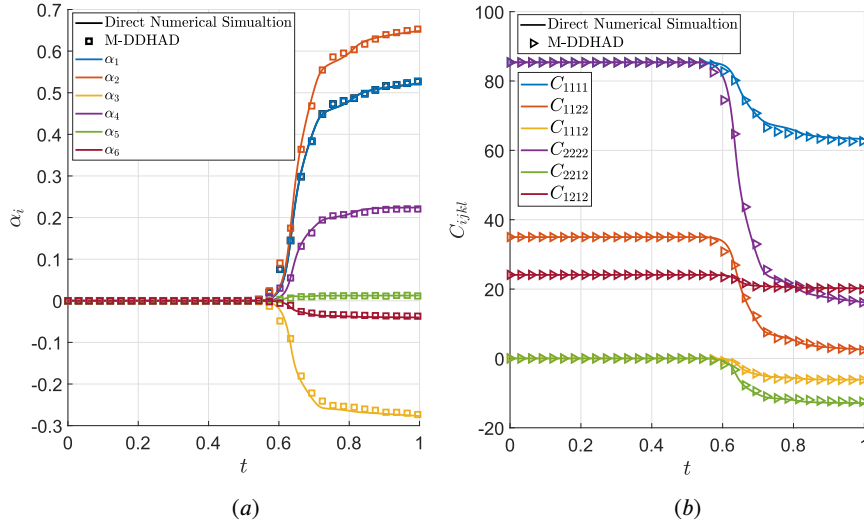


Figure 6: RVE damage evolution ($t \in [0.5, 1]$): (a) Internal variables evolution; (b) Stiffness matrix components evolution: DDHAD vs Direct Numerical Simulation.

Fig. 5 illustrates the final damage state of the RVE ($t = 1$) associated to the macroscopic strain in Eq. (51). Fig. 6a shows the evolution of internal variables $\bar{\alpha}_i(t)$ associated with the damaged RVE. On the one hand, the effective elastic tensor is computed at each time step and the internal variables are extracted from it as a reference solution using Eq. (23) and Appendix A. On the other hand, internal variables are computed with the surrogate model constructed, using the proposed M-DDHAD method. It is shown from the comparison that a very good approximation is achieved, which demonstrates that an accurate prediction of internal variables evolution is achieved when using a macroscopic strain path not included in offline computations. This result is confirmed by Fig 6b, which shows the evolution of the components of the stiffness matrix computed by direct numerical simulation and those computed according to the anisotropic damage model in Eq. (16) using the predicted evolution of internal variables.

It should be noted that, in this case, the internal variables $\bar{\alpha}_1(t)$, $\bar{\alpha}_2(t)$, $\bar{\alpha}_4(t)$ and $\bar{\alpha}_5(t)$ are positive and increasing, while $\bar{\alpha}_3(t)$ and $\bar{\alpha}_6(t)$ are negative and decreasing, which is in contrast with the previous application. In general, for a given RVE, each macroscopic strain results in a distinct evolution of these internal variables.

6.2. Notched structure with pores

The first example of multiscale damage modeling deals with crack propagation in a notched square plate with pores submitted to tensile loading. Macrostructure dimensions are $\bar{L} \times \bar{L} = 21 \times 21 \text{ mm}^2$ for the plate and $\bar{L}' \times \bar{H}' = 6.4 \times 0.05 \text{ mm}^2$ for the notch. The geometry and the boundary conditions, for the displacement problem, are depicted in Fig. 7a. The bottom end of the structure is fixed in both directions, left and right ends are blocked along the x-direction, and a distributed load \bar{U} is applied to the top end of the structure in the y-direction with constant displacement increments of $\Delta \bar{u} = 10^{-5} \text{ mm}$. The macroscopic mesh, for all examples in this work, is composed of linear triangular elements.

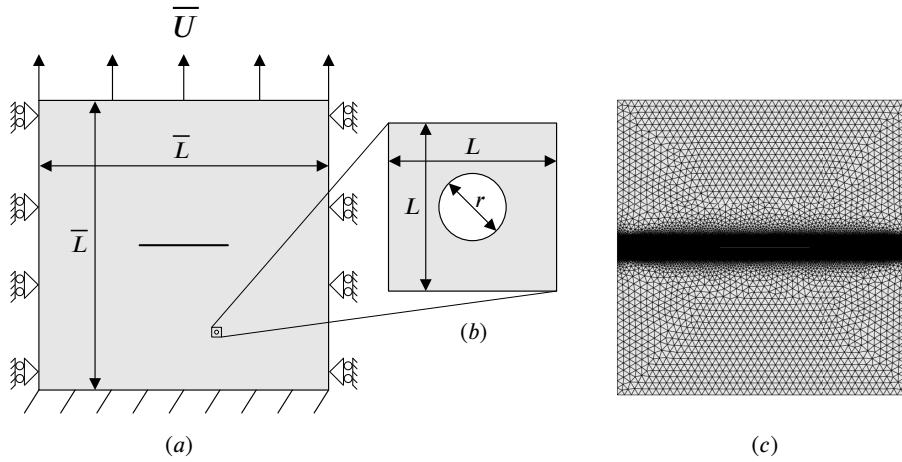


Figure 7: Notched structure with pores (homogenized structure): (a) macrostructure with boundary conditions; (b) microstructure (RVE); (c) macroscopic mesh.

The elements size, in this case, is $\bar{h}_{min} = 0.025$ mm in the crack propagation zone and $\bar{h}_{max} = 0.5$ mm in the rest of the domain (see Fig. 7c). The macroscopic characteristic length scale is chosen as $\bar{\ell}_0 = 0.1$ mm.

The microstructure is characterized by a porous square RVE of dimensions $L \times L = 1 \times 1$ mm², and the hole radius is $r = 0.2$ mm (see Fig. 7b). The mechanical properties of the microstructure matrix are as follows: $E = 52$ GPa, $\nu = 0.3$ et $\sigma_c = 30$ MPa. The microscopic mesh size is $h = 0.01$ mm. The microscopic characteristic length scale is $\ell_0 = 0.1$ mm. In this work, notches and voids in the microstructure are modeled with the mechanical properties $E = 1$ MPa, $\nu = 0$ and $\sigma_c = 0.1$ MPa. Offline damage simulations on the RVE are performed using the loading step $\Delta t = 5.10^{-3}$ (200 loading increments) with 1089 loading paths constructed from the maximum macroscopic strain:

$$\bar{\epsilon}_{max} = 10^{-4} \times \begin{bmatrix} 6 & 7 \\ 7 & 6 \end{bmatrix}. \quad (52)$$

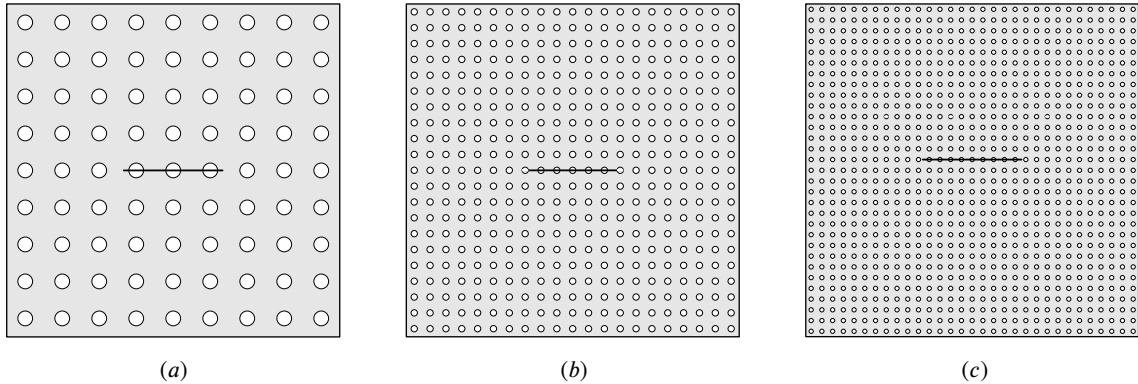


Figure 8: Notched structures with pores (Full-Field structures) with different numbers of RVEs: (a) 9×9 ; (b) 21×21 ; (c) 31×31 .

The proposed M-DDHAD method results are validated by comparison with reference computations obtained by direct simulations on full-field periodic heterogeneous structures. A crucial consideration lies in the choice of the unit cell size for conducting this comparison. In a very recent work [72], a similar study was considered. Simulations on full-field periodic structures were used to validate the proposed homogenization-based phase-field method [72]. It was demonstrated that force-displacement curves of reference structures converge to the one of the homogenized structure when decreasing the unit cell size. For this first example in this work, the validation is carried out using a fully-meshed notched porous structure as a reference, with the same geometry as the homogenized structure in Fig. 7a. The structure is composed of repeated unit cells (RVEs) in Fig. 7b with the same mechanical properties. It should be noted that, in

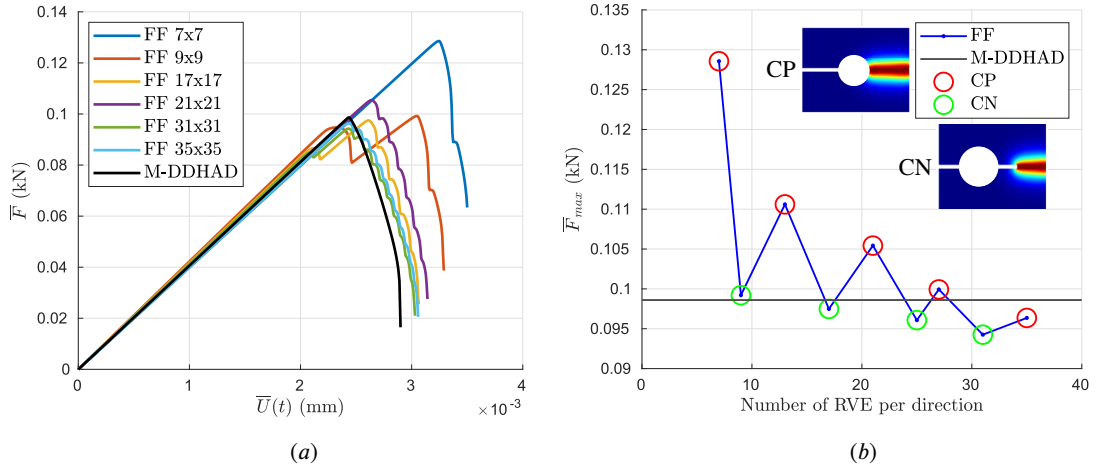


Figure 9: Convergence of the solution with respect to the number of RVEs: (a) Force-Displacement curves; (b) \bar{F}_{max} evolution (FF: full-filled, CP: crack at pore, and CN: crack at notch).

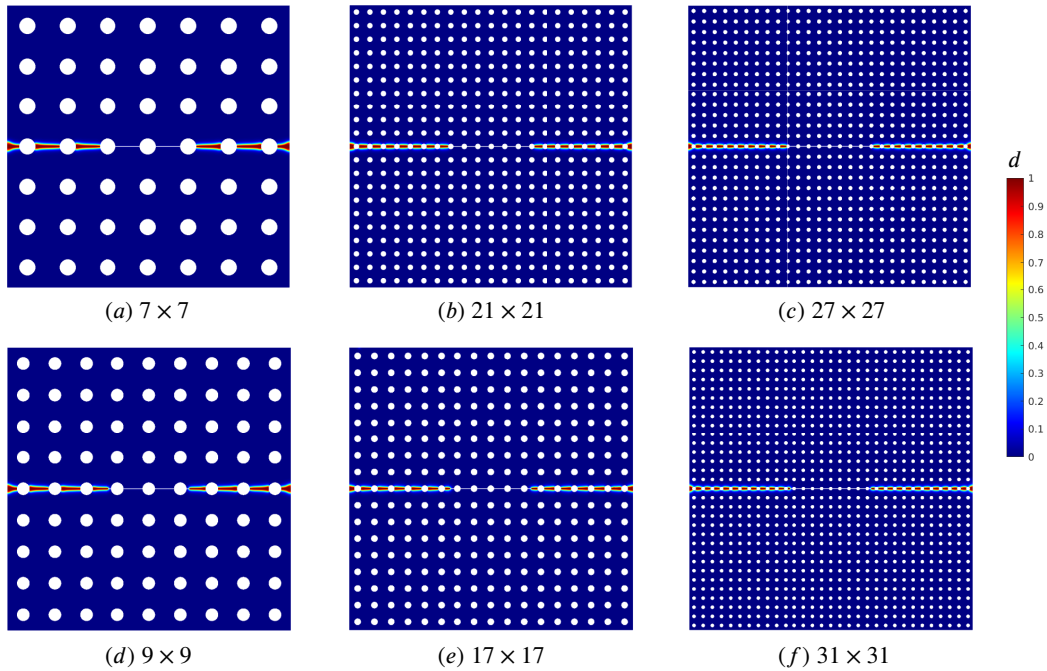


Figure 10: Final damage state of notched structures with pores (Direct Numerical Simulations) with different numbers of RVEs: (a), (b) and (c): The crack nucleates at the pore; (d), (e) and (f): The crack nucleates at the notch.

this case, depending on the number of RVEs in full-field structures, cracks can initiate at the notch or at the pore, which lead to take into account an additional factor, the location of nucleation with respect to the heterogeneities, which was not considered in [72]. Therefore, an influence study is performed here to investigate unit cell size and nucleation location effects. The aim is to confirm the findings in [72] and to ensure that the convergence is maintained despite the nucleation location effect. To this end, several full-field notched porous structures with a varying number of RVEs are considered, composed of 7×7 , 9×9 , 13×13 , 17×17 , 21×21 , 25×25 , 27×27 , 31×31 and 35×35 RVEs. The choice of the number of RVEs is made so as to have full-field structures where cracks initiate at the pore (structures with 7×7 , 13×13 , 21×21 , 27×27 and 35×35 RVEs) and others where cracks initiate at the notch. Figs. 8a, 8b and 8c show examples of three configurations of structures with 9×9 , 21×21 and 31×31 RVEs, respectively. In this work, all reference computations are carried out with structured quadrilateral mesh employing the phase field method [46, 45, 44]. The elements size in

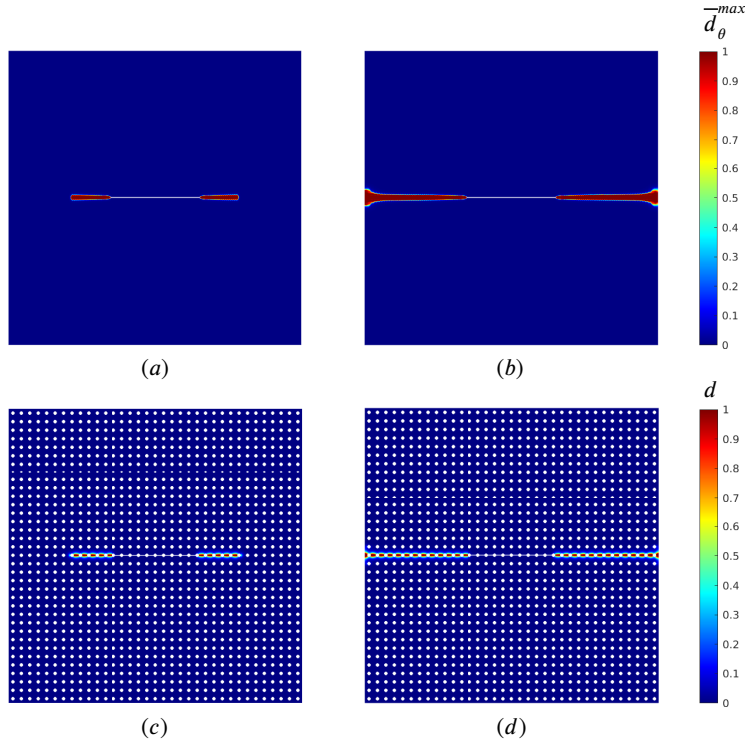


Figure 11: Damage evolution of the notched periodic structure with pores: (a) and (b) Homogenized M-DDHAD solution at displacements $\bar{U} = 2.8 \cdot 10^{-4}$ mm and $\bar{U} = 3.5 \cdot 10^{-4}$ mm, respectively; (c) and (d) DNS solution at the same displacements, respectively.

this example is $h = 0.025$ mm. The characteristic length scale is $\ell_{ff} = \bar{\ell}_0$. Simulations are performed with the same boundary conditions as the homogenized structure in Fig. 7a. Constant displacement increments of $\Delta u = 7.10^{-6}$ mm are considered.

Fig. 9a shows force-displacement curves obtained from damage simulations of full-field periodic heterogeneous structures with 7×7 , 9×9 , 17×17 , 21×21 , 31×31 and 35×35 RVEs, and the curve obtained from the homogenized structure modeling using the proposed M-DDHAD method. It is remarkable that the curves from full-field simulations converge towards the multiscale simulation curve as the number of RVEs increases. This result demonstrates that increasing enough the number of RVEs reduces the variability in the structure behavior caused by local heterogeneities, and the effective behavior of the structure is captured, which is consistent with results in [72]. This outcome is confirmed by Fig. 9b, which illustrates the evolution of the maximum force of full-field simulations as a function of the number of RVEs. The curve shows a convergence of the maximum force of the full-field simulations towards a value very close to that of the multiscale simulation with respect to the number of RVEs. It can be noticed that the curve exhibits an oscillatory behavior with respect to the number of RVEs within the structure. The observed fluctuations result from the nucleation location effect. In Fig. 9b, maximum forces associated with structures where cracks initiate at the pore are marked with red circles, while those associated with structures where cracks initiate at the notch are marked with green circles. Figs. 10a, 10b and 10c depict the final damage state of full-field structures with 7×7 , 21×21 and 27×27 RVEs, respectively. Here, the force increases until reaching a maximum value, then starts decreasing. Figs. 10d, 10e and 10f show the final state of damage of full-field structures with 9×9 , 17×17 and 31×31 RVEs, respectively. In this case, cracks initiate at the notch and propagate until reaching the first pore. This process is characterized by an initial decrease in force, followed by a continuous increase until a maximum value is achieved. This behavior is clearly observed in the curve of the full-field structure with 9×9 RVEs in Fig. 9a.

Figs. 11a and 11b show the crack evolution in the homogenized model at displacements $\bar{U} = 2.8 \cdot 10^{-3}$ mm and $\bar{U} = 3.5 \cdot 10^{-3}$ mm, where d_{θ}^{max} , the maximum of the damage orientation function $\mathbf{d}(\theta)$ with respect to the orientation θ , is represented. Similarly, Figs. 11c and 11d show the evolution of the crack in the full-field structure for the same

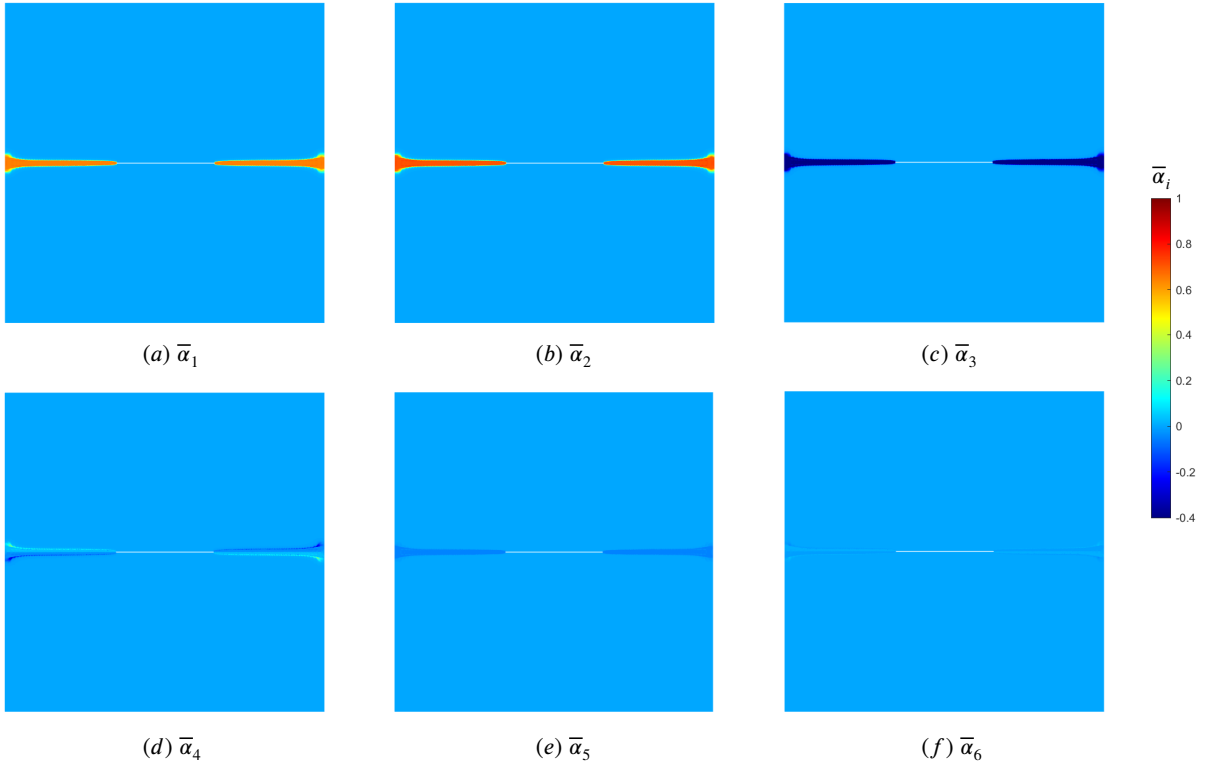


Figure 12: Notched structures with pores: Internal variables $\bar{\alpha}_i$ at the final damage state of the structure.

displacements as the homogenized structure, respectively. The evolution of cracks in both models demonstrate excellent agreement for corresponding loading increments. Fig 12 shows macroscopic internal variables $\bar{\alpha}_i$ at the final state of damage of the structure. The distinct variations in each variable are clearly observed, resulting in both positive and negative values for these variables. It should be noted that with the strain regularization of the proposed method, a fine crack and localized internal variables are obtained in the macroscopic scale. **Furthermore, a comparison of computational times between the proposed M-DDHAD approach and the reference computations is conducted for this example. This comparison is carried out using sequential algorithms with an HP Elitebook 850 G8 11th Gen computer equipped with an i7-1185G7 processor and 64 Gb of RAM. The M-DDHAD method shows a high efficiency in terms of computation time. The total number of elements used for the multiscale simulation is $N_e = 111916$, while the reference calculations employs $N_e^{ref} = 705600$. The computation times for the M-DDHAD method is $t = 36\text{min}$ and the average time of reference calculations is $t_{ref} = 11\text{h}24\text{min}$. A speed-up factor of the order of 19 has been achieved when comparing times of damage simulations in the homogenized and the fully-meshed models. These results demonstrates the computation time optimization achieved with the M-DDHAD method, while ensuring the high accuracy in predicting crack nucleation and propagation.**

In this work, a fine macroscopic mesh is used in the crack propagation zone in order to use the same characteristic length as at the microscopic scale. In general, when using a coarser macroscopic mesh, careful consideration must be given to the choice of the macroscopic characteristic length for achieving accurate results. This aspect deserves further investigation in future works.

6.2.1. Influence of the mesh size

In this analysis, the convergence of the M-DDHAD solution with respect to the mesh size is investigated. The example discussed in the previous section is considered, with the macroscopic characteristic length chosen as $\bar{\ell}_0 = 0.6$ mm. Several damage simulations of the homogenized structure are carried out using a mesh size ranging from $h_{min} = 0.4$ mm to $h_{min} = 0.02$ mm with constant displacement increments of $\Delta u = 10^{-5}$ mm. Fig. 13 illustrates force-displacement curves associated with each simulation, showing a clear converge of the solution as the mesh is refined. This result is confirmed by Fig. 14, in which the evolution of maximum force with respect to the mesh

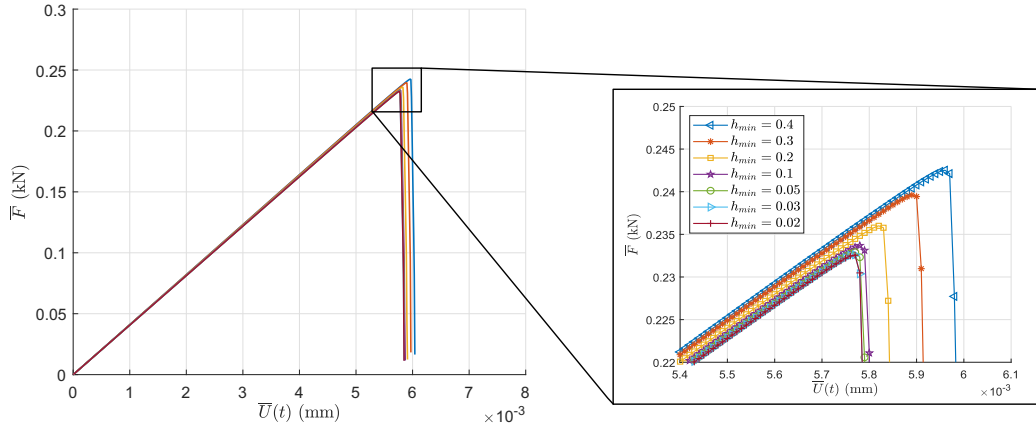


Figure 13: Convergence of the M-DDHAD solution with respect to the mesh size: Force-Displacement curves.

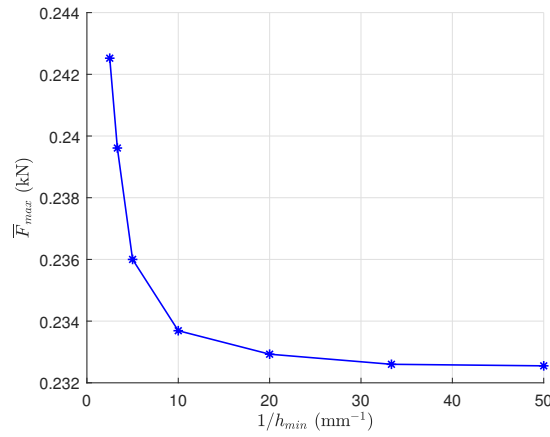


Figure 14: Convergence of the M-DDHAD solution with respect to the mesh size: \bar{F}_{max} evolution.

size is plotted. The maximum force converge as a function of the mesh size. This outcome demonstrates the mesh independancy of the problem, which is achieved through the regularization at the macroscopic scale in the proposed M-DDHAD method.

6.2.2. Influence of the loading increments

Here, the convergence of the M-DDHAD solution as a function of loading increments is analyzed. The same example as in the previous analysis is considered. In this case, the macroscopic characteristic length is $\bar{\ell}_0 = 0.1$ mm and the mesh size is $h_{min} = 0.05$ mm. Several loading increments that range from $\Delta u = 2 \cdot 10^{-4}$ mm to $\Delta u = 5 \cdot 10^{-6}$ are used. Force-displacement curves associated with each simulation are presented in Fig. 15a, which demonstrates a very good convergence of the solution as loading increments decrease. The evolution of maximum force, in Fig. 15b confirms the convergence with respect to loading increments.

6.2.3. Influence of the constructed database density

A sensitivity analysis is conducted to investigate the influence of the number of loading paths on the the M-DDHAD solution. The first example in section 6.2 is considered. Several databases are constructed using a range of loading paths number varying from 25 to 500. Fig. 16a illustrates force-displacement curves for each simulation performed using a specific database. It demonstrates a clear convergence of the solution as loading paths number increases. This outcome is confirmed by the evolution of the maximum force showed in Fig. 16b. It can be noticed that using 200 loading paths to construct the dababase for the off-line simulations allows to build an accurate surrogate model for the on-line simulations.

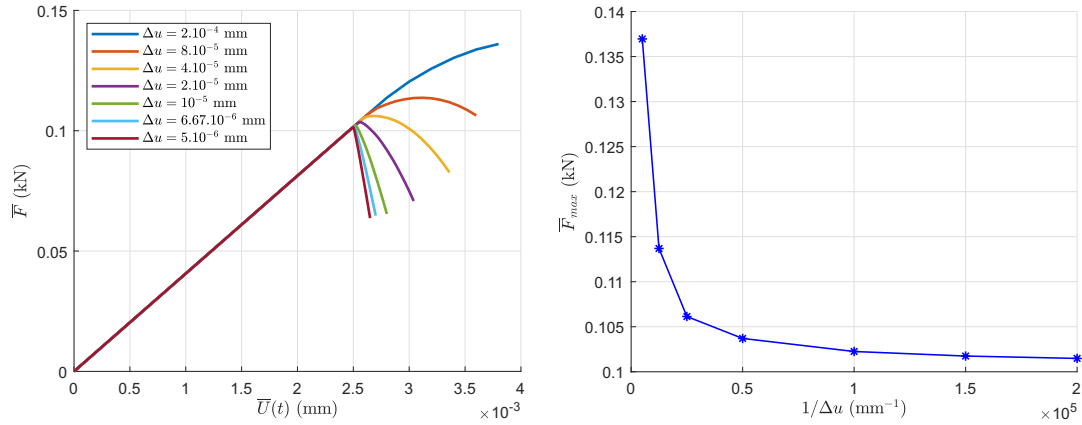


Figure 15: Convergence of the M-DDHAD solution with respect to loading increments: (a) Force-Displacement curves; (b) \bar{F}_{max} evolution.

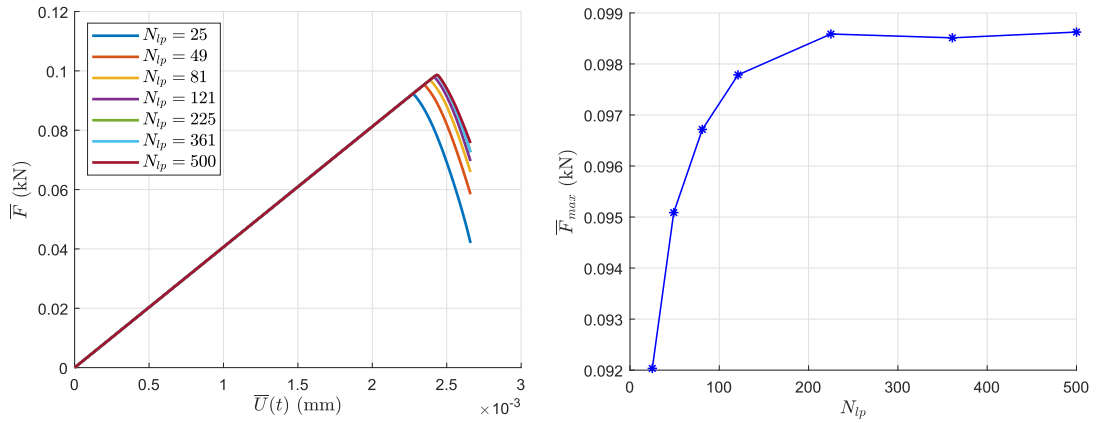


Figure 16: Convergence of the M-DDHAD solution with respect to loading paths number (N_{lp}): (a) Force-Displacement curves; (b) \bar{F}_{max} evolution.

6.3. Perforated structure with inclusions

In the second example, the crack nucleation and propagation of a perforated periodic structure with inclusions submitted to shear loading is simulated. Macrostructure dimensions are $\bar{L} \times \bar{L} = 21 \times 21$ mm 2 for the plate and $\bar{r} = 0.2\bar{L}$ mm for the hole (see Fig.17a). The bottom end of the structure is fixed in both directions to simulate a rigid support, structure left and right ends are blocked along the y-direction, and a distributed load \bar{U} is applied to the top end of the structure in the x-direction with constant displacement increments of $\Delta\bar{u} = 2.10^{-5}$ mm. The macroscopic characteristic length scale is chosen as $\bar{\ell}_0 = 0.06$ mm. The macroscopic mesh size is $\bar{h}_{min} = 0.025$ mm in the crack propagation zone and $\bar{h}_{max} = 0.5$ mm elsewhere (see Fig. 17c). In this example, the RVE and the surrogate model used for the second application in section 6.1 are considered.

Fig. 18 shows the full-field perforated structure with inclusions used to validate this case. It is composed of repeated unit cells in Fig. 17b (25 \times 25 RVEs) and where material has been removed from the central hole. The full-field structure has the same geometry and reference computations are carried out employing the same boundary conditions as the homogenized macroscopic structure in Fig. 17a. Constant displacement increments of $\Delta\bar{u} = 2.10^{-5}$ mm is considered. The characteristic length scale is $\ell_{ff} = \bar{\ell}_0$.

Fig. 19, illustrates force-displacement curves of the multiscale damage simulation and the reference computations using the full-field structure. It demonstrates an excellent agreement between both solutions and the variation between maximum forces is close to 1%. Figs. 20a and 20b show the crack evolution in the homogenized model at displacements

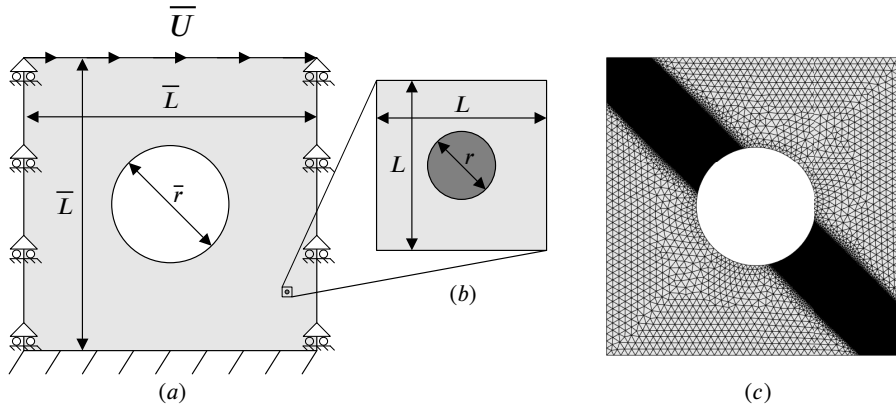


Figure 17: Perforated structure with inclusions (homogenized structure): (a) macrostructure with boundary conditions; (b) microstructure (RVE); (c) macroscopic mesh.

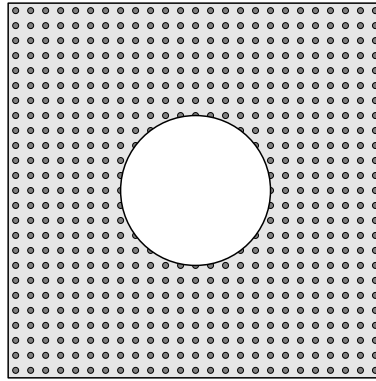


Figure 18: Perforated structure with inclusions (Full-Field structure): 25×25 RVEs.

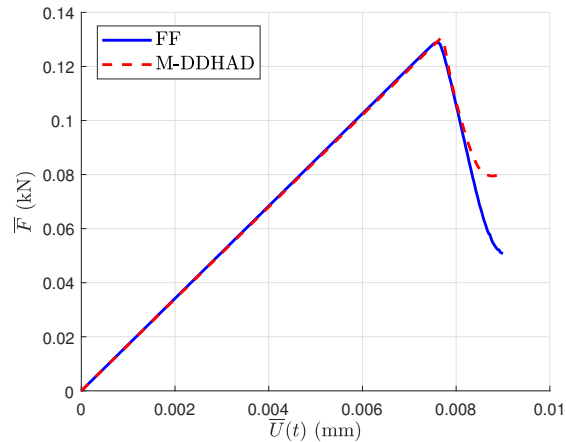


Figure 19: Perforated structure with inclusions: Force-Displacement curve.

$\bar{U} = 7.9 \cdot 10^{-3}$ mm and $\bar{U} = 9.10 \cdot 10^{-3}$ mm. Similarly, Figs. 20a and 20a show the evolution of the crack in the full-field structure for the same displacements as the homogenized structure, respectively. The evolution of cracks in both models demonstrate excellent agreement for corresponding loading increments. Fig 12 shows macroscopic internal variables $\bar{\alpha}_i$ at the final state of damage of the structure.

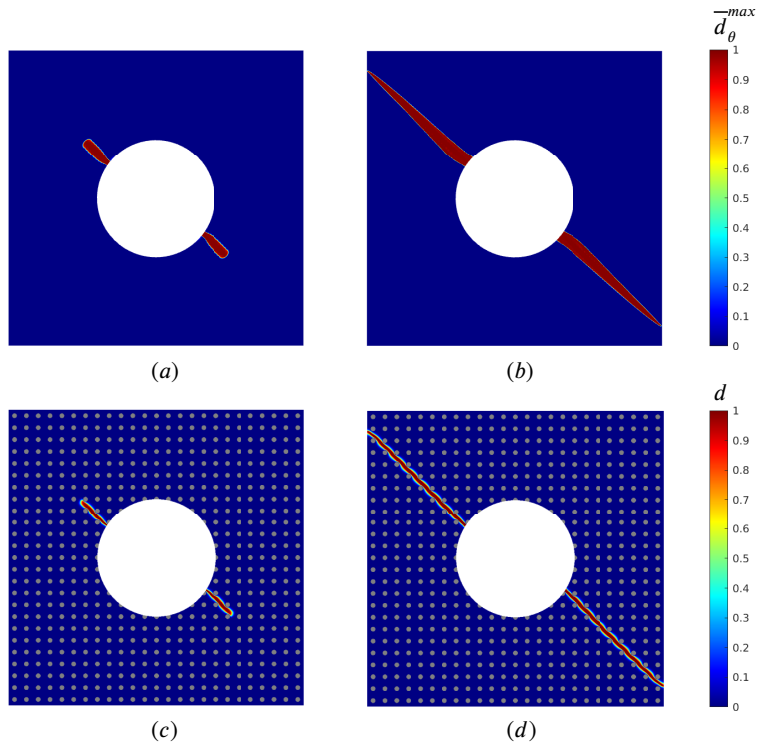


Figure 20: Damage evolution of the perforated structure with inclusions: (a) and (b) Homogenized M-DDHAD solution at displacements $\bar{U} = 7.9 \cdot 10^{-3}$ mm and $\bar{U} = 9 \cdot 10^{-3}$ mm, respectively; (c) and (d) DNS reference solution at the same displacements, respectively.

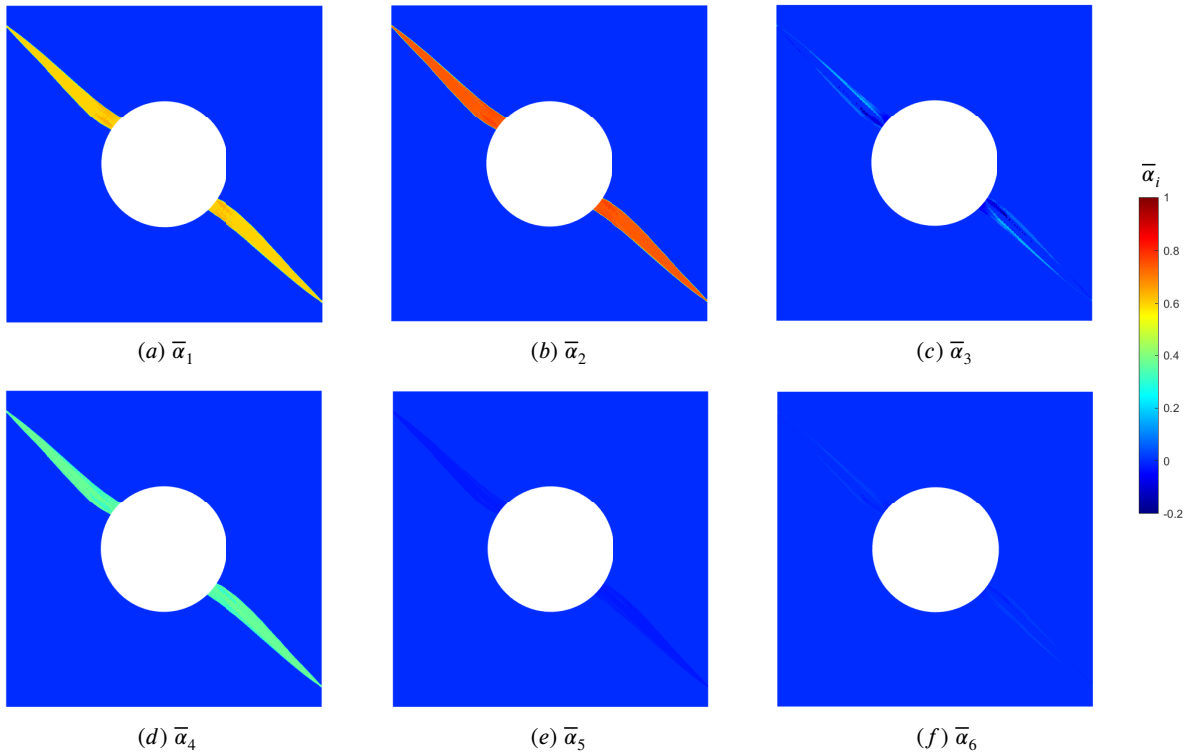


Figure 21: Perforated structure with inclusions: Internal variables $\bar{\alpha}_i$ at the final damage state of the structure.

In this example, an anisotropic behavior was observed, in which the crack propagates only in the tensile zone, without employing any split at the macroscopic scale as in the phase field method [46, 45, 44]. This significant outcome is the result of the offline calculations, which included loading paths in compression, for which no microscopic damage occurred. This choice of loading paths ensures that effects of both tensile and compressive stresses accurately captured during damage evolution.

6.4. Perforated structure with inclined layers

As a third example, the crack nucleation and propagation of a perforated periodic structure with inclined layers submitted to tensile loading is considered. The microstructure is characterized by a square RVE with a inclined layer of dimensions $L \times L = 1 \times 1 \text{ mm}^2$ for the plate, and the layer width is $e = \frac{\sqrt{2}}{4} \text{ mm}$ (see Fig. 22b). The mechanical properties of the microstructure are as follows: $E_m = 52 \text{ GPa}$, $\nu_m = 0.3$ et $\sigma_c^m = 0.1 \text{ GPa}$ for the matrix, and $E_l = 10.4 \text{ GPa}$, $\nu_l = 0.3$ et $\sigma_c^l = 0.01 \text{ GPa}$ for the layer. The microscopic mesh size is $h = 0.01 \text{ mm}$. The microscopic characteristic length scale is $\ell_0 = 0.06 \text{ mm}$. Offline damage simulations on the RVE are performed using the loading step $\Delta t = 5.10^{-3}$ (200 loading increments) with 1089 loading paths constructed from the maximum macroscopic strain:

$$\bar{\epsilon}_{max} = 10^{-3} \times \begin{bmatrix} 0.65 & 1.4 \\ 1.4 & 0.65 \end{bmatrix}. \quad (53)$$

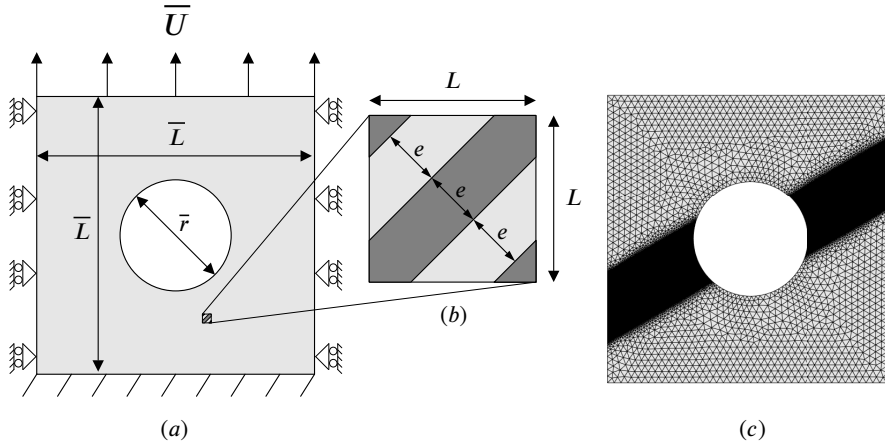


Figure 22: Perforated structure with inclined layers (homogenized structure): (a) macrostructure with boundary conditions; (b) microstructure (RVE); (c) macroscopic mesh.

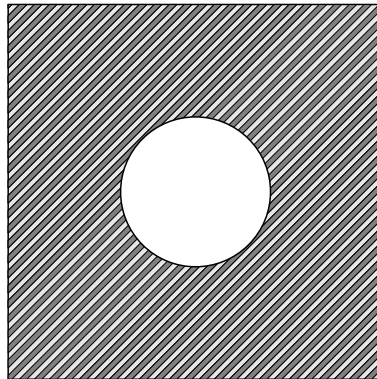


Figure 23: Perforated structure with inclined layers (Full-Field structure): 25×25 RVEs

Macrostructure dimensions are $\bar{L} \times \bar{L} = 21 \times 21 \text{ mm}^2$ for the plate and $\bar{r} = 0.2\bar{L} \text{ mm}$ for the hole (see Fig. 22a). The boundary conditions used in this example are similar to those used in the first one. Constant displacement increments of $\Delta \bar{u} = 2.10^{-5} \text{ mm}$ are considered. The macroscopic characteristic length scale is $\bar{\ell}_0 = 0.06 \text{ mm}$. The macroscopic mesh size is $\bar{h}_{min} = 0.03 \text{ mm}$ in the crack propagation zone and $\bar{h}_{max} = 0.5 \text{ mm}$ elsewhere (see Fig. 22c).

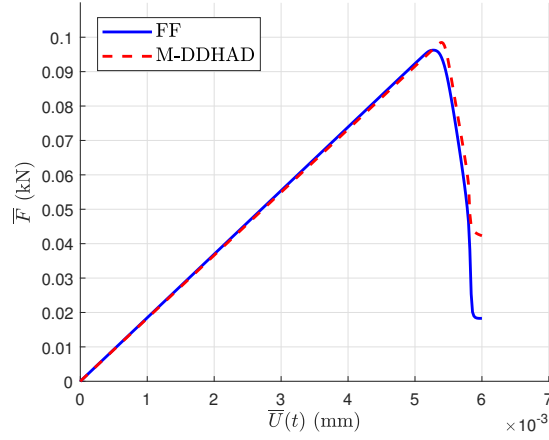


Figure 24: Perforated structure with inclined layers: Force-Displacement curve.

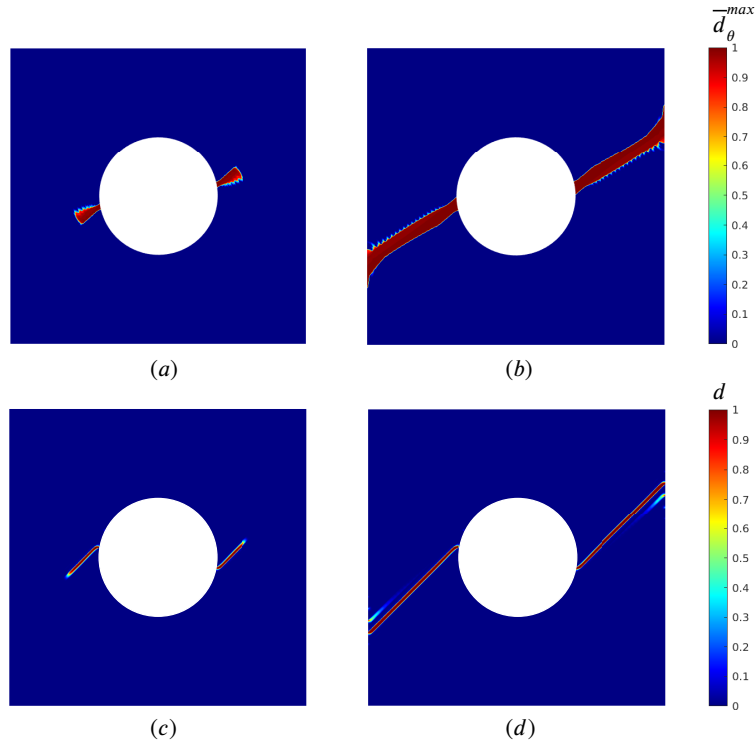


Figure 25: Damage evolution of the perforated structure with inclined layers: (a) and (b) homogenized M-DDHAD solution at displacements $\bar{U} = 5.3 \cdot 10^{-3} \text{ mm}$ and $\bar{U} = 7 \cdot 10^{-3} \text{ mm}$, respectively; (c) and (d) DNS reference solution at the same displacements, respectively.

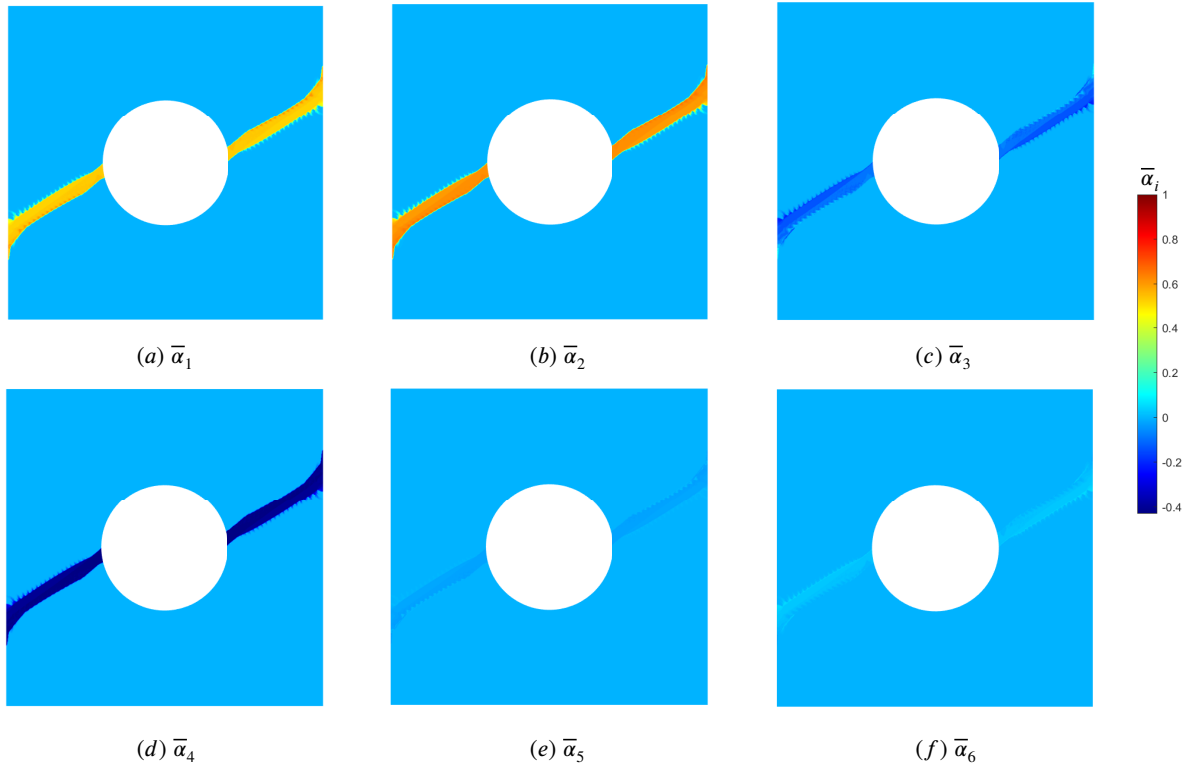


Figure 26: Perforated structure with inclined layers: Internal variables $\bar{\alpha}_i$ at the final damage state of the structure.

Results of this example are validated using the full-field perforated structure with inclined layers depicted in Fig. 23. It is composed of repeated unit cells in Fig. 22b (25×25 RVEs) with the same mechanical properties. The full-field structure has the same geometry as the homogenized macroscopic structure in Fig. 22a and computations are carried out employing the same boundary conditions. The characteristic length scale is $\ell_{ff} = \bar{\ell}_0$. Constant displacement increments of $\Delta \bar{u} = 2.10^{-5}$ mm are considered.

Fig. 24, illustrates force-displacement curves of the multiscale damage simulation and the reference computations. It shows a very good agreement between both solutions and the difference between maximum forces is below 3%. Figs. 25a and 25b show the crack evolution in the homogenized model at displacements $\bar{U} = 5.5 \cdot 10^{-3}$ mm and $\bar{U} = 6 \cdot 10^{-3}$ mm. Similarly, Figs. 25a and 25a show the evolution of the crack in the full-field structure for the same displacements as the homogenized structure, respectively. The evolution of cracks in both models demonstrates a relatively good agreement for corresponding loading increments. Fig 12 shows macroscopic internal variables $\bar{\alpha}_i$ at the final state of damage of the structure.

In this example, the geometry and material properties of the RVE are chosen so that cracks initiate and propagate in the inclined layers. Cracks orientation at the microscopic scale is effectively transferred to the macroscopic scale. As a result, the macrostructure behavior is influenced by the direction of crack propagation at the microstructure level and an inclined crack is initiated and propagated, rather than the horizontal crack. It must be noted that the crack propagation angle is smaller than 45° for the M-DDHAD approach. Also, the position of the crack nucleation in the homogenized model is slightly different from that of the full-field structure. These results show that the proposed M-DDHAD method captures well the anisotropy induced by the microstructure and is capable of accurately simulating the behavior of complex heterogeneous structures.

Only a single fiber orientation was considered in the examples within this work. Future works could focus on incorporating multiple fiber orientations within the same simulation to capture the damage behavior of more complex and realistic structures. This extension could be achieved by introducing additional parameters into the surrogate model, not only incorporating fiber orientation, but potentially using multiple RVEs. Furthermore, it is possible to investigate stochastic multiscale simulation to consider the variability in the microstructure.

6.5. Perforated structure with vertical layers

For the last example, the crack nucleation and propagation of a perforated periodic structure with vertical layers submitted to tensile loading is considered. Macrostructure dimensions are $\bar{L} \times \bar{L} = 21 \times 21 \text{ mm}^2$ for the plate and $\bar{r} = 0.2\bar{L} \text{ mm}$ for the hole (see Fig.27a). The boundary conditions used in this example are similar to those used in section 6.2. A constant displacement increments of $\Delta\bar{u} = 2.5 \cdot 10^{-5} \text{ mm}$ is considered. The macroscopic characteristic length scale is $\bar{\ell}_0 = 0.06 \text{ mm}$. The macroscopic mesh size is $\bar{h}_{min} = 0.03 \text{ mm}$ in the crack propagation zone and $\bar{h}_{max} = 0.5 \text{ mm}$ elsewhere (see Fig. 27c).

The microstructure is characterized by a square RVE with a vertical layer of dimensions $L \times l = 1 \times 1 \text{ mm}^2$ for the plate, and the layer width is $e = 0.1 \text{ mm}$ (see Fig. 27b). The mechanical properties of the microstructure are as follows: $E_m = 52 \text{ GPa}$, $\nu_m = 0.3$ et $\sigma_c^m = 0.1 \text{ GPa}$ for the matrix, and $E_l = 10.4 \text{ GPa}$, $\nu_l = 0.3$ et $\sigma_c^l = 0.01 \text{ GPa}$ for the layer. The microscopic mesh consists of elements of size $h = 0.01 \text{ mm}$. The microscopic characteristic length scale is $\ell_0 = 0.06 \text{ mm}$. Offline damage simulations on the RVE are performed using the loading step $\Delta t = 5 \cdot 10^{-3}$ (200 loading increments) with 500 loading paths constructed from the maximum macroscopic strain:

$$\bar{\varepsilon}_{max} = 10^{-4} \times \begin{bmatrix} 3.5 & 6 \\ 6 & 7 \end{bmatrix}. \quad (54)$$

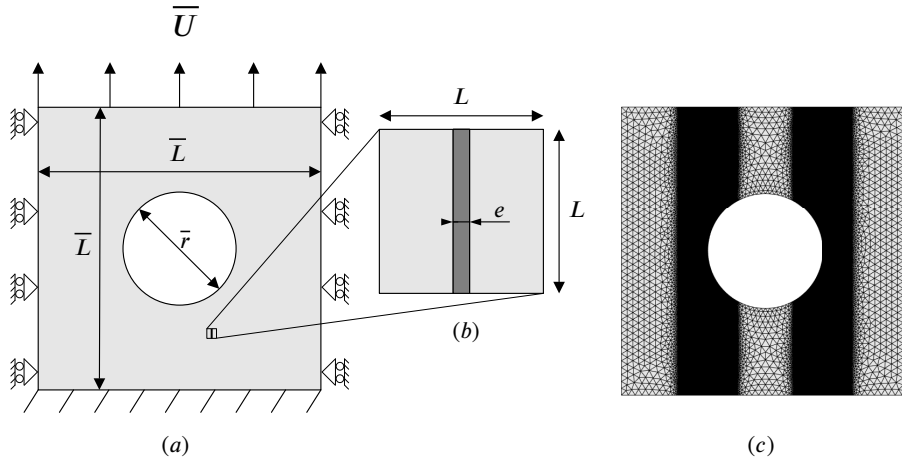


Figure 27: Perforated structure with vertical layers (homogenized structure): (a) macrostructure with boundary conditions; (b) microstructure (RVE); (c) macroscopic mesh.

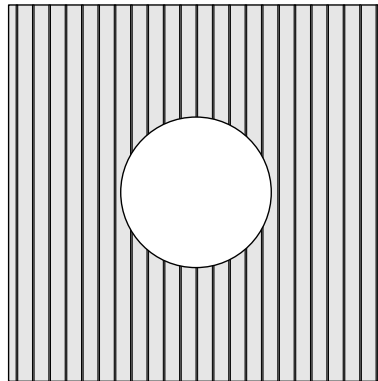


Figure 28: Perforated structure with vertical layers (Full-Field structure): 23×23 RVEs

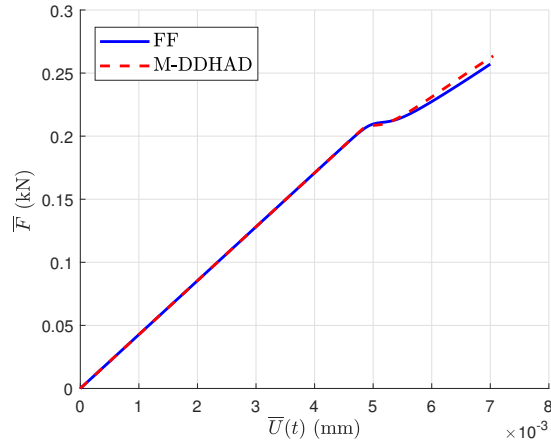


Figure 29: Perforated structure with vertical layers: Force-Displacement curve.

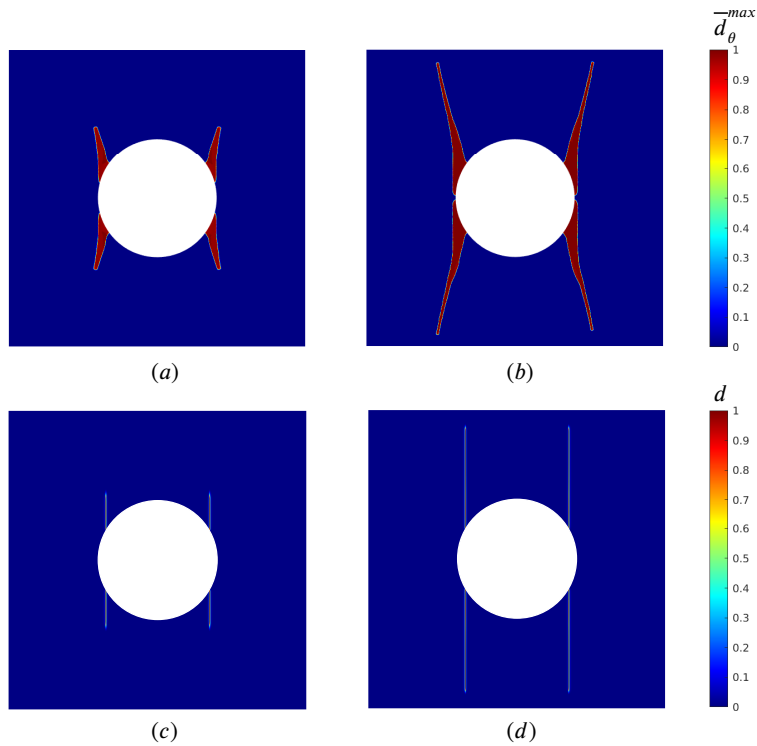


Figure 30: Damage evolution of the perforated structure with vertical layers: (a) and (b) homogenized M-DDHAD solution at displacements $\bar{U} = 5.3 \cdot 10^{-3}$ mm and $\bar{U} = 7 \cdot 10^{-3}$ mm, respectively; (c) and (d) DNS reference solution at the same displacements, respectively.

Fig. 28 shows the full-field Perforated structure with vertical layers used to validate this case. It consists of repeated unit cells in Fig. 22b (23×23 RVEs) with the same mechanical properties. The full-field structure has the same geometry and reference computations are carried out employing the same boundary conditions as the homogenized macroscopic structure in Fig. 27a. Constant displacement increments of $\Delta \bar{u} = 2 \cdot 10^{-5}$ mm are considered. The characteristic length scale is $\ell_{ff} = \ell_0$.

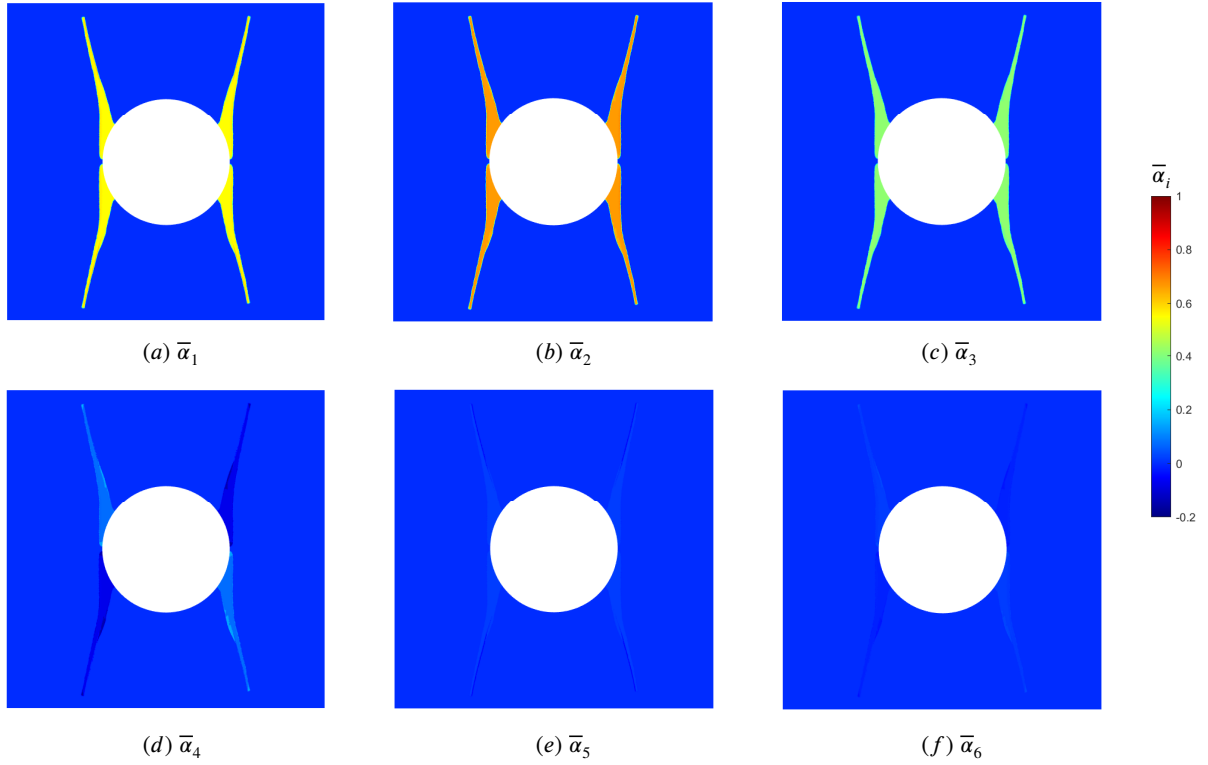


Figure 31: Perforated structure with vertical layers: Internal variables $\bar{\alpha}_i$ at the final damage state of the structure.

Fig. 29, illustrates force-displacement curves of the multiscale damage simulation and the reference computations. Figs. 30a and 30b show the crack evolution in the homogenized model at displacements $\bar{U} = 5.3 \cdot 10^{-3}$ mm and $\bar{U} = 7.10^{-3}$ mm. Similarly, Figs. 20a and 20a show the evolution of the crack in the full-field structure for the same displacements as the homogenized structure, respectively. The evolution of cracks in both models demonstrate excellent agreement for corresponding loading increments. Fig 12 shows macroscopic internal variables $\bar{\alpha}_i$ at the final state of damage of the structure.

In this example, similarly to the previous one, the geometry and material properties of the RVE are chosen so that cracks initiate and propagate in the vertical layer. Despite the fact that tensile loading is vertical, crack propagation is also vertical, in contrast with the horizontal crack of an isotropic damage model. The vertical orientation of the crack at the microscopic scale is well captured at the macroscopic scale even though a slight inclination is observed in the homogenized model. A very good agreement is noticed between the force-displacement curves of reference and homogenized solutions in Fig. 29. After the linear elastic response, during which the structure is not yet damaged, a slight decrease in force is observed. Then, it increases again. This behavior is due to the vertical propagation of cracks. In fact, the structure undergoes a partial degradation while retaining a large part of its stiffness. Interestingly, the location of crack nucleation around the central hole agree very well in this case. These outcomes demonstrate the effectiveness of the proposed M-DDHAD approach in capturing anisotropic damage solely based on the microstructure influence, without requiring any additional assumptions at the macroscopic scale.

7. Conclusion

An efficient data-driven multiscale modelling framework of anisotropic damage (M-DDHAD) method has been introduced, where the homogenized anisotropic damage model is constructed purely on the knowledge of Representative Volume Elements (RVE) of the material microstructure. The technique involves three main steps: (i) the construction of a database, obtained by performing off-line calculations of crack propagation in Representative Volume Elements (RVE); (ii) the construction of an anisotropic damage model constructed from the data-base using Harmonic Analysis of Damage; (iii) Off-line calculations, where damage is computed using the constructed model in tandem with a strain-gradient regularization technique.

The first step involves crack phase field simulations on RVEs of microstructures with arbitrary geometries. A collection of proportional loads is defined in the macro strain space. For each load step along these paths, crack propagation is simulated with phase field. A numerical homogenization method is used to compute the corresponding homogenized elastic tensor. In a second step, the macroscopic model is constructed from the database. Using Harmonic Analysis of Damage, an anisotropic damage model defining the evolution of the macroscopic elastic tensor as a function of macro internal variables is defined without specific assumptions about the anisotropy related to the RVE geometry. The macro internal variables are extracted for each homogenized elastic tensor in the database. Then, an interpolation technique in the macro strain space is carried out to define their evolution. A simplified technique is proposed to ensure irreversibility of the anisotropic damage. Finally, in a third step, the macro damage evolution is computed using the constructed model. The macroscopic problem uses the constructed anisotropic damage model, and a strain-gradient regularization is applied to guarantee mesh-independence.

The technique accuracy and robustness has been assessed on several structural problems with different microstructures, involving a strong anisotropic fracture behavior. To evaluate the accuracy of the method, the results obtained from the macro (homogenized) model have been compared with direct numerical simulations (DNS) of structures where all the microstructural details have been finely meshed. Very good accuracy has been obtained both regarding the force-displacement curves as well as crack paths. Remarkably, the method is able to capture initial as well as induced anisotropic damage during the evolution of the macro loading. For strongly oriented microstructures, the corresponding macro crack direction is well captured. Mesh-independence has been validated. As another important feature of the method, there is no need to define a strain decomposition at the macro level to guarantee that cracks occur only in traction. In the method, off-line loading paths involve compressive path, where the microstructure can be subjected to complex triaxial compressive mechanical states. Then, the model automatically captures if micro damage occurs in these situation or not, depending on the microstructure, and captures in the construction of the macro internal variables evolution laws interpolated in the database. Finally, the method is efficient, as no coupling between the macro and micro scales, such as in FE² method, is needed. **A speed-up factor of the order of 19 has been achieved when comparing times of damage simulations in the homogenized and the fully-meshed models.**

Some points still deserve improvements and constitute perspective for this work, including handling non-proportional loads, extensions to 3D, and the selection of the macro regularization length scale.

8. Acknowledgments

The authors gratefully acknowledge the financial support from the LABEX Multi-Scale Modeling & Experimentation of Materials for Sustainable Construction (MMCD) through ANR Investments for the Future program ANR- 585 11-LABX-022-01.

A. Appendix: formulation of spherical harmonics in 2D

In 2D, parametrizing \mathbf{n} by the angle θ in polar coordinates as $n_1 = \cos(\theta)$, $n_2 = \sin(\theta)$:

$$d_0(t) = \frac{1}{2\pi} \int_{-\pi}^{\pi} d(\theta, t) d\theta, \quad h_0(t) = \frac{1}{2\pi} \int_{-\pi}^{\pi} h(\theta, t) d\theta, \quad (55)$$

\mathbf{D} and \mathbb{D} are specified by [25] as:

$$\mathbf{D} = \frac{2}{\pi} \int_{-\pi}^{\pi} d(\theta, t) \mathbf{F}(\theta) d\theta, \quad \mathbb{D} = \frac{8}{\pi} \int_{-\pi}^{\pi} d(\theta, t) \mathbb{F}(\theta) d\theta, \quad (56)$$

where $\mathbf{F}(\theta)$ is given by

$$\mathbf{F}(\theta) = \mathbf{N} - \frac{1}{2} \mathbf{I}, \quad (57)$$

with $\mathbf{N} = \mathbf{n} \otimes \mathbf{n}$ and \mathbf{I} being the second-order identity tensor. Finally, the fourth-order generalized harmonic tensor $\mathbb{F}(\theta)$ is given in [25, 76] as follows:

$$\mathbb{F}(\theta) = \mathbf{N} \otimes \mathbf{N} - \frac{1}{6} \left(\mathbf{I} \otimes \mathbf{N} + \mathbf{N} \otimes \mathbf{I} + \mathbf{I} \overline{\otimes} \mathbf{N} + \mathbf{N} \overline{\otimes} \mathbf{I} \right) + \frac{1}{24} \left(\mathbf{I} \otimes \mathbf{I} + \mathbf{I} \overline{\otimes} \mathbf{I} \right) \quad (58)$$

where the product $\left(\mathbf{A} \overline{\otimes} \mathbf{B} \right)_{ijkl} = (A_{ik} B_{jl} + A_{il} B_{jk})$.

B. Appendix: tensor expressions in DDHAD model

Eq. (16) can be re-written in the vector form:

$$[\bar{\mathbf{C}}(\boldsymbol{\alpha})] = [\bar{\mathbf{C}}^0] - \tilde{\mathbf{C}} \cdot \boldsymbol{\alpha} \quad (59)$$

where $[\bar{\mathbf{C}}(\boldsymbol{\alpha})]$ is a (6×1) vector containing the components of $\bar{\mathbf{C}}$ as:

$$[\bar{\mathbf{C}}]^T = [\bar{C}_{1111} \ \bar{C}_{1122} \ \bar{C}_{1112} \ \bar{C}_{2222} \ \bar{C}_{2212} \ \bar{C}_{1212}]. \quad (60)$$

In this notation, $[\bar{\mathbf{C}}^0]$ is similar than $[\bar{\mathbf{C}}]$ but contains the components of $\bar{\mathbf{C}}^0$. Furthermore, $\tilde{\mathbf{C}}$ is a (6×6) matrix with the vectors \mathbf{C}^{ijkl} as columns as:

$$\tilde{\mathbf{C}} = [\mathbf{C}^{1111} \ \mathbf{C}^{1122} \ \mathbf{C}^{1112} \ \mathbf{C}^{2222} \ \mathbf{C}^{2212} \ \mathbf{C}^{1212}], \quad (61)$$

where the different (6×1) vectors \mathbf{C}^{ijkl} are given by the expressions [77]:

$$\mathbf{C}^{1111} = \mathbf{a} + \mathbf{V}^{11} + \mathbf{Z}^{1111}, \quad \mathbf{C}^{1122} = \mathbf{b} - \mathbf{a} - \mathbf{Z}^{1111}, \quad \mathbf{C}^{1112} = \frac{1}{2}\mathbf{V}^{12} + \mathbf{Z}^{1112} \quad (62)$$

$$\mathbf{C}^{2222} = \mathbf{a} - \mathbf{V}^{11} + \mathbf{Z}^{1111}, \quad \mathbf{C}_{2212} = \frac{1}{2}\mathbf{V}^{12} - \mathbf{Z}^{1112}, \quad \mathbf{C}^{1212} = \mathbf{a} - \frac{1}{2}\mathbf{b} - \mathbf{Z}^{1111} \quad (63)$$

with

$$\mathbf{a} = \frac{1}{2\pi} \int_{-\pi}^{\pi} \eta_0(\theta) \mathbf{V}^d(\theta) d\theta, \quad \mathbf{b} = \frac{1}{2\pi} \int_{-\pi}^{\pi} \kappa_0(\theta) \mathbf{V}^h(\theta) d\theta, \quad (64)$$

$$\mathbf{V}^{pq} = \frac{2}{\pi} \int_{-\pi}^{\pi} \eta_0(\theta) F_{pq}(\theta) \mathbf{V}^d(\theta) d\theta, \quad \mathbf{Z}^{pqrs} = \frac{8}{\pi} \int_{-\pi}^{\pi} \eta_0(\theta) F_{pqrs}(\theta) \mathbf{V}^d(\theta) d\theta, \quad (65)$$

and

$$\mathbf{V}^d(\theta) = \begin{bmatrix} 1 \\ 0 \\ F_{11}(\theta) - F_{22}(\theta) \\ 2F_{12}(\theta) \\ F_{1111}(\theta) - 2F_{1122}(\theta) + F_{2222}(\theta) - 4F_{1212}(\theta) \\ 4F_{1112}(\theta) - 4F_{2212}(\theta) \end{bmatrix}, \quad \mathbf{V}^h(\theta) = \begin{bmatrix} 0 \\ 1 \\ F_{11}(\theta) - F_{22}(\theta) \\ 2F_{12}(\theta) \\ 0 \\ 0 \end{bmatrix}. \quad (66)$$

References

- [1] A. D. Amaro, A. F. C. Alves, and F. A. Pires. Multi-scale modelling and analysis of the behaviour of pc/abs blends with emphasis on interfacial/bulk damage. *Finite Elements in Analysis and Design*, 229:104083, 2024.
- [2] M. A. Benaïmeche, J. Yvonnet, B. Bary, and Q.-C. He. A k-means clustering machine learning-based multiscale method for anelastic heterogeneous structures with internal variables. *International Journal for Numerical Methods in Engineering*, 123(9):2012–2041, 2022.
- [3] R. Bharali, F. Larsson, and R. Jänicke. Computational homogenisation of phase-field fracture. *European Journal of Mechanics-A/Solids*, 88:104247, 2021.
- [4] M. Bhattacharyya, A. Fau, R. Desmorat, S. Alameddini, D. Néron, P. Ladeveze, and U. Nackenhorst. A kinetic two-scale damage model for high-cycle fatigue simulation using multi-temporal Latin framework. *European Journal of Mechanics-A/Solids*, 77:103808, 2019.
- [5] E. Bosco, V. Kouznetsova, and M. Geers. Multi-scale computational homogenization–localization for propagating discontinuities using XFEM. *International Journal for Numerical Methods in Engineering*, 102(3-4):496–527, 2015.
- [6] B. Bourdin, G. A. Francfort, and J.-J. Marigo. Numerical experiments in revisited brittle fracture. *Journal of the Mechanics and Physics of Solids*, 48(4):797–826, 2000.
- [7] S. Chaouch and J. Yvonnet. An unsupervised machine learning approach to reduce nonlinear FE2 multiscale calculations using macro clustering. *Finite Elements in Analysis and Design*, 229:104069, 2024.
- [8] S. Chaouch and J. Yvonnet. Unsupervised machine learning classification for accelerating fe2 multiscale fracture simulations. *Computer Methods in Applied Mechanics and Engineering*, 432:117278, 2024.
- [9] H. B. Dhia. Multiscale mechanical problems: the Arlequin method. *Comptes Rendus de l'Académie des Sciences Series IIB Mechanics Physics Astronomy*, 12(326):899–904, 1998.
- [10] H. B. Dhia and G. Rateau. The Arlequin method as a flexible engineering design tool. *International journal for numerical methods in engineering*, 62(11):1442–1462, 2005.
- [11] D. Dureisseix and H. Bavestrello. Information transfer between incompatible finite element meshes: application to coupled thermo-viscoelasticity. *Computer Methods in Applied Mechanics and Engineering*, 195(44-47):6523–6541, 2006.
- [12] F. Fantoni, A. Bacigalupo, M. Paggi, and J. Reinoso. A phase field approach for damage propagation in periodic microstructured materials. *International Journal of Fracture*, 223:53–76, 2020.
- [13] F. Feyel. Multiscale FE2 elastoviscoplastic analysis of composite structures. *Computational Materials Science*, 16(1-4):344–354, 1999.
- [14] F. Feyel and J.-L. Chaboche. FE2 multiscale approach for modelling the elastoviscoplastic behaviour of long fibre SiC/Ti composite materials. *Computer methods in applied mechanics and engineering*, 183(3-4):309–330, 2000.
- [15] M. Geers, R. De Borst, W. Brekelmans, and R. Peerlings. Strain-based transient-gradient damage model for failure analyses. *Computer methods in applied mechanics and engineering*, 160(1-2):133–153, 1998.
- [16] L. Gendre, O. Allix, P. Gosselet, and F. Comte. Non-intrusive and exact global/local techniques for structural problems with local plasticity. *Computational Mechanics*, 44:233–245, 2009.
- [17] T. Gerasimov, N. Noh, O. Allix, and L. De Lorenzis. A non-intrusive global/local approach applied to phase-field modeling of brittle fracture. *Advanced modeling and simulation in engineering sciences*, 5:1–30, 2018.
- [18] F. Ghavamian and A. Simone. Accelerating multiscale finite element simulations of history-dependent materials using a recurrent neural network. *Computer Methods in Applied Mechanics and Engineering*, 357:112594, 2019.
- [19] L. Gigliotti and S. Pinho. Multiple length/time-scale simulation of localized damage in composite structures using a Mesh Superposition Technique. *Composite Structures*, 121:395–405, 2015.
- [20] O. Goury, D. Amsallem, S. P. A. Bordas, W. K. Liu, and P. Kerfriden. Automated selection of load paths to construct reduced-order models in computational damage micromechanics: from dissipation-driven random selection to Bayesian optimization. *Computational Mechanics*, 58:213–234, 2016.
- [21] P.-A. Guidault, O. Allix, L. Champaney, and C. Cornuault. A multiscale extended finite element method for crack propagation. *Computer Methods in Applied Mechanics and Engineering*, 197(5):381–399, 2008.
- [22] J. Guillemot and J. E. Dolbow. Data-driven enhancement of fracture paths in random composites. *Mechanics Research Communications*, 103:103443, 2020.
- [23] P. Gupta, J. Pereira, D.-J. Kim, C. Duarte, and T. Eason. Analysis of three-dimensional fracture mechanics problems: A non-intrusive approach using a generalized finite element method. *Engineering Fracture Mechanics*, 90:41–64, 2012.
- [24] Q.-C. He and A. Curnier. A more fundamental approach to damaged elastic stress-strain relations. *International Journal of Solids and Structures*, 32(10):1433–1457, 1995.
- [25] Q.-C. He and A. Curnier. Characterising a 2d elasticity tensor by two orientation distribution functions. In *IUTAM Symposium on Anisotropy, Inhomogeneity and Nonlinearity in Solid Mechanics: Proceedings of the IUTAM-ISIMM Symposium held in Nottingham, UK, 30 August–3 September 1994*, pages 25–30. Springer, 1995.
- [26] T. Hou, X.-H. Wu, and Z. Cai. Convergence of a multiscale finite element method for elliptic problems with rapidly oscillating coefficients. *Mathematics of Computation*, 68(227):913–943, 1999.
- [27] T. Y. Hou and X.-H. Wu. A Multiscale Finite Element Method for Elliptic Problems in Composite Materials and Porous Media. *Journal of Computational Physics*, 134(1):169–189, 1997-06.
- [28] M. Jaque-Zurita, J. Hinojosa, and I. Fuenzalida-Henríquez. Global–Local Non Intrusive Analysis with 1D to 3D Coupling: Application to Crack Propagation and Extension to Commercial Software. *Mathematics*, 11(11):2540, 2023.
- [29] M. Jones. *Spherical Harmonics and Tensors for Classical Field Theory*. Research Studies Press, 1985.
- [30] A. Khan, N. Kim, J. K. Shin, H. S. Kim, and B. D. Youn. Damage assessment of smart composite structures via machine learning: a review. *JMST Advances*, 1:107–124, 2019.
- [31] P. Ladeveze. Sur une théorie de l'endommagement anisotrope. rapport interne n. 34. *Laboratoire de Mécanique et Technologie, Cachan*, 1983.

- [32] P. Ladevèze. *Nonlinear computational structural mechanics: new approaches and non-incremental methods of calculation*. Springer Science & Business Media, 2012.
- [33] P. Ladevèze and D. Dureisseix. Une nouvelle stratégie de calcul micro/macro en mécanique des structures. *Comptes Rendus de l'Académie des Sciences-Series IIB-Mechanics-Physics-Astronomy*, 327(12):1237–1244, 1999.
- [34] P. Ladevèze and D. Dureisseix. A micro/macro approach for parallel computing of heterogeneous structures. *International Journal for Computational Civil and Structural Engineering*, 1:18–28, 2000.
- [35] P. Ladevèze, O. Loiseau, and D. Dureisseix. A micro–macro and parallel computational strategy for highly heterogeneous structures. *International Journal for Numerical Methods in Engineering*, 52(1-2):121–138, 2001.
- [36] P. Ladevèze, J.-C. Passieux, and D. Néron. The latin multiscale computational method and the proper generalized decomposition. *Computer Methods in Applied Mechanics and Engineering*, 199(21-22):1287–1296, 2010.
- [37] B. Le, J. Yvonnet, and Q.-C. He. Computational homogenization of nonlinear elastic materials using neural networks. *International Journal for Numerical Methods in Engineering*, 104(12):1061–1084, 2015.
- [38] B. Li and X. Zhuang. Multiscale computation on feedforward neural network and recurrent neural network. *Frontiers of Structural and Civil Engineering*, 14(6):1285–1298, 2020.
- [39] H. Liu, S. Liu, Z. Liu, N. Mrad, and H. Dong. Prognostics of damage growth in composite materials using machine learning techniques. In *2017 IEEE international conference on industrial technology (ICIT)*, pages 1042–1047. IEEE, 2017.
- [40] H. J. Logarzo, G. Capuano, and J. J. Rimoli. Smart constitutive laws: Inelastic homogenization through machine learning. *Computer methods in applied mechanics and engineering*, 373:113482, 2021.
- [41] X. Lu, J. Yvonnet, F. Detrez, and J. Bai. Modélisation électromécanique non linéaire multi-échelle de nanocomposites graphène-polymère. *Nanocomposites: Préparation, caractérisation et modélisation*, pages 167–198, 2021.
- [42] X. Lu, J. Yvonnet, L. Papadopoulos, I. Kalogeris, and V. Papadopoulos. A stochastic FE2 data-driven method for nonlinear multiscale modeling. *Materials*, 14(11):2875, 2021.
- [43] F. Masi and I. Stefanou. Multiscale modeling of inelastic materials with Thermodynamics-based Artificial Neural Networks (TANN). *Computer Methods in Applied Mechanics and Engineering*, 398:115190, 2022.
- [44] C. Miehe, M. Hofacker, L.-M. Schänzel, and F. Aldakheel. Phase field modeling of fracture in multi-physics problems. Part II. Coupled brittle-to-ductile failure criteria and crack propagation in thermo-elastic–plastic solids. *Computer Methods in Applied Mechanics and Engineering*, 294:486–522, 2015.
- [45] C. Miehe, L.-M. Schänzel, and H. Ulmer. Phase field modeling of fracture in multi-physics problems. Part I. Balance of crack surface and failure criteria for brittle crack propagation in thermo-elastic solids. *Computer Methods in Applied Mechanics and Engineering*, 294:449–485, 2015.
- [46] C. Miehe, F. Welschinger, and M. Hofacker. Thermodynamically consistent phase-field models of fracture: Variational principles and multi-field FE implementations. *International journal for numerical methods in engineering*, 83(10):1273–1311, 2010.
- [47] E. Monteiro, J. Yvonnet, and Q.-C. He. Computational homogenization for nonlinear conduction in heterogeneous materials using model reduction. *Computational Materials Science*, 42(4):704–712, 2008.
- [48] S. Nakasumi, K. Suzuki, and H. Ohtsubo. Crack growth analysis using mesh superposition technique and X-FEM. *International journal for numerical methods in engineering*, 75(3):291–304, 2008.
- [49] S. Nasiri and M. R. Khosravani. Applications of data-driven approaches in prediction of fatigue and fracture. *Materials Today Communications*, 33:104437, 2022.
- [50] L. H. Nguyen and D. Schilling. The multiscale finite element method for nonlinear continuum localization problems at full fine-scale fidelity, illustrated through phase-field fracture and plasticity. *Journal of Computational Physics*, 396:129–160, 2019.
- [51] N. Nguyen, J. Yvonnet, J. Réthoré, and A. B. Tran. Identification of fracture models based on phase field for crack propagation in heterogeneous lattices in a context of non-separated scales. *Computational Mechanics*, 63:1047–1068, 2019.
- [52] T. H. N. Nguyen. *Contributions to multiscale modelling of quasi-brittle damage in heterogeneous materials*. PhD thesis, Université Paris-Est, 2019.
- [53] T. T. Nguyen, J. Yvonnet, Q.-Z. Zhu, M. Bornert, and C. Chateau. A phase field method to simulate crack nucleation and propagation in strongly heterogeneous materials from direct imaging of their microstructure. *Engineering Fracture Mechanics*, 139:18–39, 2015.
- [54] V. P. Nguyen, O. Lloberas-Valls, M. Stroeven, and L. J. Sluys. Homogenization-based multiscale crack modelling: from micro-diffusive damage to macro-cracks. *Computer Methods in Applied Mechanics and Engineering*, 200(9-12):1220–1236, 2011.
- [55] V. P. Nguyen, O. Lloberas-Valls, M. Stroeven, and L. J. Sluys. Computational homogenization for multiscale crack modeling. Implementational and computational aspects. *International Journal for Numerical Methods in Engineering*, 89(2):192–226, 2012.
- [56] J. Oliver, M. Caicedo, A. E. Huespe, J. Hernández, and E. Roubin. Reduced order modeling strategies for computational multiscale fracture. *Computer Methods in Applied Mechanics and Engineering*, 313:560–595, 2017.
- [57] C. Oliver-Leblond, A. Delaplace, F. Ragueneau, and B. Richard. Non-intrusive global/local analysis for the study of fine cracking. *International Journal for Numerical and Analytical Methods in Geomechanics*, 37(8):973–992, 2013.
- [58] J. W. Park, J. W. Hwang, and Y. H. Kim. Efficient finite element analysis using mesh superposition technique. *Finite elements in analysis and design*, 39(7):619–638, 2003.
- [59] R. Patil, B. Mishra, and I. Singh. A new multiscale XFEM for the elastic properties evaluation of heterogeneous materials. *International Journal of Mechanical Sciences*, 122:277–287, 2017.
- [60] R. Patil, B. Mishra, and I. Singh. An adaptive multiscale phase field method for brittle fracture. *Computer Methods in Applied Mechanics and Engineering*, 329:254–288, 2018.
- [61] R. Patil, B. Mishra, and I. Singh. A multiscale framework based on phase field method and XFEM to simulate fracture in highly heterogeneous materials. *Theoretical and Applied Fracture Mechanics*, 100:390–415, 2019.

- [62] R. H. Peerlings, R. de Borst, W. M. Brekelmans, and J. de Vree. Gradient enhanced damage for quasi-brittle materials. *International Journal for numerical methods in engineering*, 39(19):3391–3403, 1996.
- [63] J. Reiner. Finite element analysis combined with machine learning to simulate open-hole strength and impact tests of fibre-reinforced composites. *International Journal of Computational Methods*, page 2241005, 2023.
- [64] J. Reiner, R. Vaziri, and N. Zobeiry. Machine learning assisted characterisation and simulation of compressive damage in composite laminates. *Composite Structures*, 273:114290, 2021.
- [65] A. Sellitto, R. Borrelli, F. Caputo, A. Riccio, and F. Scaramuzzino. Application of the mesh superposition technique to the study of delaminations in composites thin plates. *Key Engineering Materials*, 525:533–536, 2013.
- [66] M. Silani, H. Talebi, A. M. Hamouda, and T. Rabczuk. Nonlocal damage modelling in clay/epoxy nanocomposites using a multiscale approach. *Journal of Computational Science*, 15:18–23, 2016.
- [67] M. Silani, H. Talebi, S. Ziaei-Rad, A. M. Hamouda, G. Zi, and T. Rabczuk. A three dimensional extended Arlequin method for dynamic fracture. *Computational Materials Science*, 96:425–431, 2015.
- [68] S. P. Triantafyllou and E. G. Kakouris. A generalized phase field multiscale finite element method for brittle fracture. *International Journal for Numerical Methods in Engineering*, 121(9):1915–1945, 2020.
- [69] J. Wu, H. Zhang, and Y. Zheng. A concurrent multiscale method for simulation of crack propagation. *Acta Mechanica Sinica*, 28(3):235–251, 2015.
- [70] J.-Y. Wu, Y. Huang, and V. P. Nguyen. On the BFGS monolithic algorithm for the unified phase field damage theory. *Computer Methods in Applied Mechanics and Engineering*, 360:112704, 2020.
- [71] S. Yan, X. Zou, M. Ilkhani, and A. Jones. An efficient multiscale surrogate modelling framework for composite materials considering progressive damage based on artificial neural networks. *Composites Part B: Engineering*, 194:108014, 2020.
- [72] J. Yuan, S. He, C. Chen, and L. Wang. Phase-field fracture analysis of heterogeneous materials based on homogenization method. *Acta Mechanica*, 235(2):1083–1107, 2024.
- [73] J. Yvonnet. *Computational homogenization of heterogeneous materials with finite elements*, volume 258. Springer, 2019.
- [74] J. Yvonnet, D. Gonzalez, and Q.-C. He. Numerically explicit potentials for the homogenization of nonlinear elastic heterogeneous materials. *Computer Methods in Applied Mechanics and Engineering*, 198(33-36):2723–2737, 2009.
- [75] J. Yvonnet and Q.-C. He. The reduced model multiscale method (R3M) for the non-linear homogenization of hyperelastic media at finite strains. *Journal of Computational Physics*, 223(1):341–368, 2007.
- [76] J. Yvonnet, Q.-C. He, and P. Li. A data-driven harmonic approach to constructing anisotropic damage models with a minimum number of internal variables. *Journal of the Mechanics and Physics of Solids*, 162:104828, 2022.
- [77] J. Yvonnet, Q.-C. He, and P. Li. Reducing internal variables and improving efficiency in data-driven modelling of anisotropic damage from RVE simulations. *Computational Mechanics*, 72(1):37–55, 2023.
- [78] H.-W. Zhang, J.-K. Wu, J. Lü, and Z.-D. Fu. Extended multiscale finite element method for mechanical analysis of heterogeneous materials. *Acta Mechanica Sinica*, 26(6):899–920, 2010.
- [79] K. Zhang, L.-h. Ma, Z.-z. Song, H. Gao, W. Zhou, J. Liu, and R. Tao. Strength prediction and progressive damage analysis of carbon fiber reinforced polymer-laminate with circular holes by an efficient Artificial Neural Network. *Composite Structures*, 296:115835, 2022.